# Quantification of groundwater storage heterogeneity in weathered/fractured basement rock aquifers using electrical resistivity tomography: sensitivity and uncertainty associated with petrophysical modelling

Jesús Alberto Mézquita González[1*], Jean-Christophe Comte[1], Anatoly Legchenko[2], Ulrich Ofterdinger[3], David Healy[1]

[1]University of Aberdeen, School of Geosciences, UK

[2]Univ. of Grenoble Alps, Institute of Research for Development, IGE, Grenoble, France

[3]Queen's University Belfast, Northern Ireland, UK

*Corresponding author: J. A. Mézquita González, School of Geosciences, University of Aberdeen, Aberdeen, AB24 3UF. E-mail: j.mezquita@abdn.ac.uk

**Abstract:** Quantifying groundwater storage in weathered/fractured basement rock aquifers can be challenging owing to both their high degree of heterogeneity and their overall low storage capacity. Therefore, in these aquifers, the use of direct borehole hydraulic data is usually insufficient. Here we assessed the popular method of electrical resistivity tomography (ERT), combined with borehole data and including associated uncertainties, to resolve the spatial variability of groundwater storage properties at high resolution within a fractured mica schist aquifer in Ireland. Porosity distributions across both the saturated and unsaturated zones were calculated from two-dimensional (2D) ERT resistivities using two standard petrophysical models, Archie and Waxman & Smits (WS), the latter accounting for the influence of clay minerals on resistivity data. Our results demonstrated the importance of the hydrogeological conceptual constraints provided by ERT when parametrizing the 2D petrophysical models from borehole point data. They also confirmed the importance of accounting for clay minerals (the products of bedrock weathering processes) in the WS model, whereas predictions from Archie's model produced unrealistically high porosity values of over an order of magnitude higher than the WS model. The WS model predicted porosities decreasing exponentially

with depth, with values ranging from a few % in the shallowest, most-weathered part of the bedrock (upper 5 m on average) and deep fractured zones (to about 20 m deep), to less than 1% in the underlying fissured aquifer, and possibly down another order of magnitude in the deep massive bedrock. WS-derived porosities were in agreement with independent vertical water content profiles derived from magnetic resonance sounding (MRS), as well as point storativity values estimated from borehole hydraulic testing at the study site, with particularly good matches in the upper weathered/fractured bedrock and deeply weathered/fractured zones associated with regional faults. Detailed comparison suggested that WS provides an upper-bound estimate of groundwater storage in this environment. In the deep massive, un-weathered, and poorly fractured bedrock, however, discrepancies between groundwater storage estimate obtained from the three methods (ERT, MRS, and hydraulic) prevented reliable storage quantification, owing to the methods' inherent technical limitations in such low porosity rocks. Our results demonstrated the suitability of resistivity tomography to quantify groundwater storage heterogeneity in weathered/fractured basement rock aquifers at high resolution and with reasonable overall uncertainty given the relative high uncertainties in petrophysical parameters at the kilometric scale. The results are promising for better characterization of groundwater storage variations in these hydrogeological systems, which are crucial to predict their response to climate variability and human exploitation.

**Keywords:** Hydrogeophysics; Hard rock aquifer; Petrophysics; Clays; Porosity; Storativity.

## 1. Introduction

More than 90% of the total liquid fresh water is groundwater (Gleick, 1993) with a fraction of this water being stored in weathered/fractured basement rocks. Basement rock aquifers, including igneous and metamorphic rocks, are devoid of primary porosity and groundwater flow and storage take place through fractures and secondary porosity created by weathering processes. They are also often referred to as hard rock aquifers (Lachassagne et al., 2011). Some authors however also included under the definition of hard rock aquifers cemented sedimentary rocks (which can exhibit primary porosity) and hard carbonate rocks (which can also exhibit primary porosity and karstification) because of their similarly poor drillability, but these are not considered here. Basement, hard rock aquifers cover a fifth of the Earth's land surface (Singhal, 2008) and locally constitute socio-economically and ecologically important water resources. The distribution and overall volume of water contained in these reservoirs are the least known primarily because of their high degree of heterogeneity and overall low productivity (Comte et al., 2012a). It is however acknowledged that most of groundwater flow and storage take place at a relatively shallow depth within the most weathered/fractured bedrock (Abdulaziz et al., 2012; Kumar et al., 2016). Such shallow depths of interest (tens of meters) make near-surface geophysical techniques suitable to characterize and understand weathered/fractured basement rock aquifers (Day-Lewis et al., 2017).

Until recently, the difficulties to locate and extract water from basement rock aquifers implied that they have been largely disregarded for water supply outside local rural use (MacDonald and Davies, 2000; Singhal, 2008). However, as a source more resilient than surface water to the predicted impact of climate change, basement rock aquifers, similarly to better known, more productive regional aquifer system, could play a strategic role in sustaining local drinking water supplies in an adaptation to predicted long-term climate change trends and short-term extreme drought events (Taylor et al., 2013). Therefore, new developments in basement rock aquifers characterization and sustainable exploitation are key for water security in the near future.

Understanding the function of weathered/fractured hard rock groundwater systems requires a good characterization of the complex geology, including structural heterogeneity such as fracture systems

78 and weathering that characterize this type of aquifers (Lachassagne et al., 2001, 2011). There have
79 been a significant amount of studies in this field (Ahmed et al., 2008; Singhal and Gupta, 2010;
80 Ofterdinger et al. 2019), all of which stress the need to improve the knowledge and characterizations
81 of hard rock reservoirs in terms of spatial distributions of hydrodynamic properties at appropriate
82 scales (Butler, 2005; Lachassagne et al., 2014). This type of water source is not as productive as
83 sedimentary, karstic or volcanic aquifers however it is geographically widespread (Dewandel et al.,
84 2011) which makes it well suited to be a fresh water source for farms, villages as well as small and
85 medium size cities (Lachassagne et al., 2011).

86 Hard rock aquifers are characterized by low to null primary porosity and permeability (Singhal,
87 2008). Thus, aquifer productivity is mainly linked to fracturing and weathering processes producing a
88 secondary porosity and secondary permeability (Krásný and Sharp, 2007). The hydrogeological
89 structure of hard rock aquifers is commonly divided in three conceptual horizons; from top to bottom
90 (1) a weathered zone with a thickness of up to several tens of meters commonly referred to as
91 saprolite; (2) a fractured zone with depths of a few to hundreds of meters characterized by well-
92 connected fractures/fissures networks in which the permeability and porosity decrease with depth; and
93 (3) a massive zone usually formed by a massive bedrock with low density of poorly connected
94 fractures and faults acting more as individual flow paths rather than an interconnected network
95 (Krásný et al., 2014).

96 Geophysical methods are fast, flexible, non-invasive techniques suitable to characterize the spatial
97 variations of subsurface geological structures and hydrogeological properties at various scales and
98 resolutions including in the near surface (Rubin and Hubbard, 2005; Binley et al., 2015), i.e. the first
99 100 m that typically host hard rock aquifers (Lachassagne, 2008). One of the main advantages of
100 using geophysics resides in their abilities to provide high resolution, near continuous (Spatial and or
101 temporal) information, instead of only dealing with point data (discrete) typically associated with
102 traditional hydrology studies.

103 The relationship between geophysical measurements and reservoir properties through the use of
104 petrophysical models has been the focus of much work specifically in the oil industry (Ellis and

105 Singer, 2007; Kirsch, 2009; Tiab and Donaldson, 2016) and their application in groundwater studies
106 have been rapidly increasing in the last two decades, which has defined the emergence of an
107 interdisciplinary research field called Hydrogeophysics (Binley et al., 2015; Day-Lewis et al., 2017).
108 A variety of research studies have successfully applied geophysics to solve different quantitative
109 problems in hydrology (Vereecken et al., 2006) and some other used these approaches specifically to
110 model petrophysical properties in carbonate aquifers (Whitman and Yeboah-Forson, 2015) and hard
111 rock aquifers (Descloitres et al., 2008) providing further quantitative information on the aquifer
112 properties including storage properties (porosity, specific yield) and recharge processes.

113 Very few studies have combined different geophysical methods to model hydraulic properties in
114 complex hard rock aquifers and even less have assessed the uncertainty of these properties (Massuel
115 et al., 2006; Slater, 2007; Chaudhuri et al., 2013;). Electrical resistivity tomography (ERT) is suitable
116 for weathered/fractured aquifer characterization (Pellerin, 2002), particularly to constrain reservoir
117 geometries i.e. to estimate the thickness and variability of weathered (laminated layer) and fractured
118 horizons as well as localized deep fractures zones (Chaudhuri et al., 2013; Belle et al., 2019) or as a
119 monitoring tool for salt tracer tests in complex hard rock systems (Robert et al., 2012). Only a few
120 studies have assessed the relation of geophysical measurements (resistivity and conductivity) with
121 hydraulic properties (porosity and water saturation) in hard rock aquifers due to their complexity and
122 lack for information on petrophysical model input parameters (Leopold et al., 2013; Flinchum et al.,
123 2018, 2019).

124 This study aimed at assessing the capabilities of the popular ERT technique to quantify the spatial
125 variability of aquifer storage properties in weathered/fractured rock aquifers with high resolution. The
126 study uses *in situ* ERT data from a 1,305 m hillslope transect obtained in a mica schist aquifer in
127 Ireland as an analog for basement rock aquifers. Two alternative petrophysical models were
128 considered to estimate porosity from measured resistivities with the aid of complementary *in situ*
129 information, used for both model parameterization and verification. These data included multi-depth
130 borehole hydraulic data and geophysical logging along with information on the vertical distribution of
131 aquifers' water content as obtained from magnetic resonance sounding, MRS (Legchenko et al., 2017;

Comte et al., 2019). Specifically, this research builds on, and uses in situ data and conceptual knowledge acquired from previous work at the site over the past decade. Comte et al. (2012a) established the aquifer conceptual model including hillslope spatial variability and lateral continuity of weathering profiles, through combining the ERT and borehole hydraulic data with groundwater level monitoring. Caulfield et al. (2014) performed petrographic and mineralogical analyses of borehole cores along with groundwater chemistry to further highlight modern weathering processes and weathering controls on groundwater contribution to surface water. Legchenko et al. (2017) applied Magnetic Resonance Sounding (MRS) to provide estimates, with associated uncertainties, of vertical groundwater storage profiles at several locations along the hillslope. Comte et al. (2019) reconciled previous hydrogeological, ERT, and MRS water content data and further integrated them into a numerical groundwater model to test and verify the conceptual model, including groundwater flow pathways and residence times, against spatiotemporal hydrological monitoring data (groundwater level time series and groundwater ages). These works, in addition to provide relevant data for the present study, suggested a high heterogeneity of groundwater storage, and highlighted the challenges associated with achieving storage characterization and high enough spatial resolution required for better understanding basement rock groundwater regimes and resources response to both short term and long term climate and anthropogenic forcing. In this present study, we therefore focused on a detailed quantitative assessment of the resolution and reliability, including sensitivity and uncertainty analysis, of ERT-derived groundwater storage estimates using popular petrophysical models, along with additional geological information and constraints (conceptual hydrogeological units, water saturation, clay content), and we further verify the results again independent groundwater storage data.

Thus, the specific objectives of this work were: (1) to model the 2D spatial distribution of the aquifer petrophysical properties based on 1D borehole data and the structural-conceptual information provided by the interpretation of 2D electrical resistivity data; (2) produce 2D porosity models from the combination of resistivity and petrophysical parameters distributions within the Archie and Waxman & Smits models; and (3) quantify the sensitivity of the petrophysical models and the

uncertainty of the final aquifer porosity models (expected to be considerable due to larger parameter uncertainty associated to large scale studies), and further verify them against independent geophysical water content estimates and borehole hydraulic data.

## 2. Hydrogeological setting

The studied aquifer is located in County Donegal, Ireland. (Fig. 1). The Gortinlieve catchment is an upland basin with permanent stream flow, underlain by Precambrian psammites and mica schist of the Dalradian Southern Highland Group and composed of quartz, muscovite, chlorite, albite with secondary minerals such as calcite and iron oxides (Caulfield et al., 2014). The bedrock is covered in places by overburden deposits of glacial till, alluvium, and thin soil/peat layer (Fig. 2). In 2006, the Irish Environmental Protection Agency drilled three borehole clusters (Table 1) as part of a national groundwater monitoring program. They were distributed along the study area at strategic locations that comprehended three elevations (GO1 at 174 m a.m.s.l.; GO2 at 88 m a.m.s.l.; GO3 at 33 m a.m.s.l.) within the catchment (Comte et al., 2012a, 2019; Moe et al., 2010). A first interpretation carried by Moe et al., (2010) identified four hydrogeological units, subsoil (1-3 m below ground surface), transition zone (4-5 m b.g.s.), shallow bedrock (8-19 m b.g.s.) and deep bedrock (30-67 m b.g.s.). Average monthly temperatures fluctuate from 6-14°C with an annual rainfall of 1000-1200 mm (Caulfield et al., 2014). See Comte et al. (2012a, 2019) for a detailed description of hydraulic tests and interpretations.

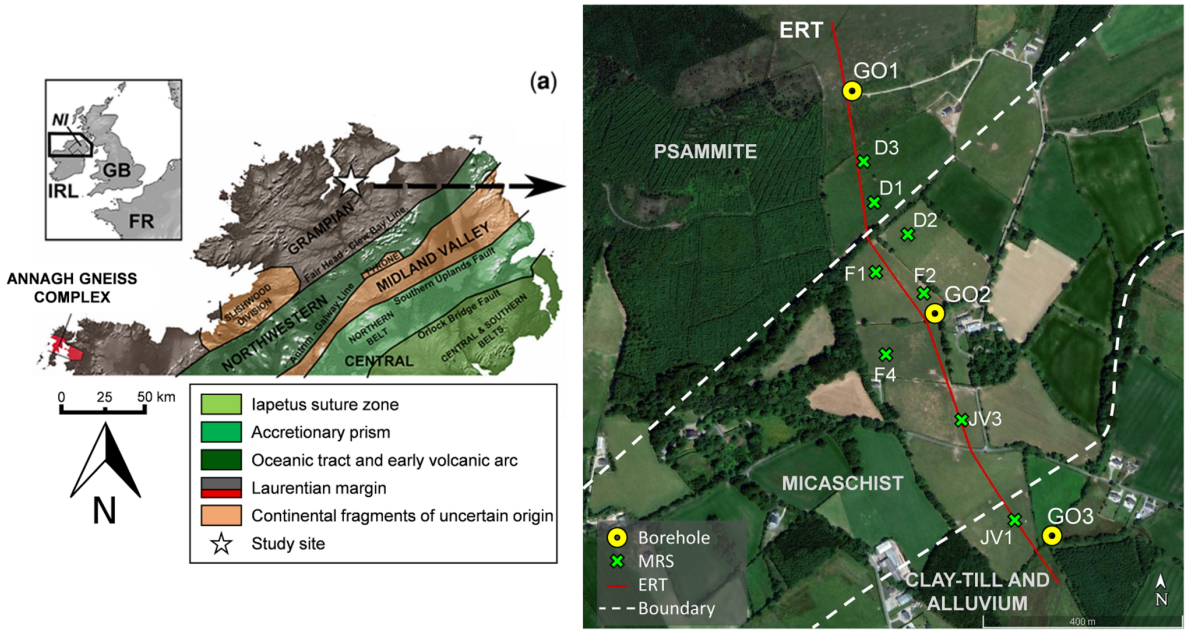


178

179 **Figure 1.** Location of the study site. (a) Site location within the geological framework of the Irish

180 basement. (b) Borehole locations and ERT profile, modified from *Comte et al. (2019)*.

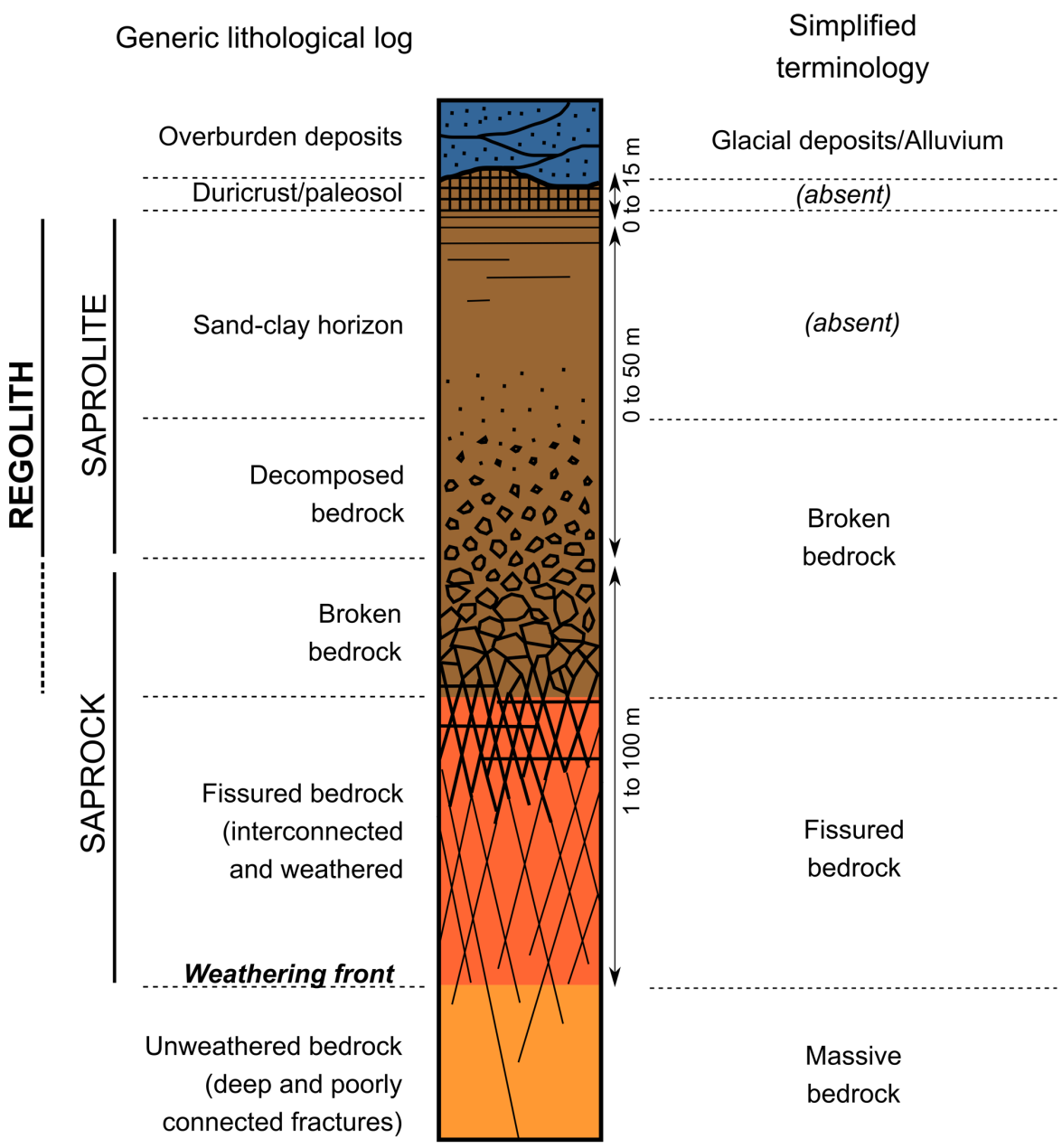


181

182 **Figure 2.** Hydrogeological conceptual model of weathered/fractured rock aquifers in the context of

183 Irish terminology. Modified from *Comte et al. (2012a)*

184

185

186

187

## 3. Data and methods

### 3.1. *Petrophysical relationship between resistivity and porosity*

The resistivity measurements were the main inputs in the petrophysical modelling used for porosity calculation. The two petrophysical models used in this study were based on Archie's law (Archie, 1942) and its extension developed by Waxman & Smits (1968). Archie describes a relationship between the electrical conductivity of a clay-free rock, its porosity, and the electrical conductivity of the fluid saturating the pores. Archie´s Law is expressed as

$$R_t = \frac{a\, R_w}{\phi^m\, {S_w}^n} \qquad (1)$$

where $\boldsymbol{R_t}$ is the formation resistivity (ohm.m), $\boldsymbol{\phi}$ is the fractional pore volume, i.e. the porosity (-), $\boldsymbol{S_w}$ is the fraction of pores containing water, i.e. the saturation (-), $\boldsymbol{R_w}$ (ohm.m) is the water resistivity, and $\boldsymbol{a}$, $\boldsymbol{m}$ and $\boldsymbol{n}$ are empirical constants known as tortuosity, cementation exponent and saturation exponent respectively. These constants are dimensionless.

To account for clay mineral electrical properties, several studies have proposed empirical modifications of Archie and the most commonly accepted was proposed by Waxman & Smits (1968). The Waxman & Smits equation includes additional parameters to quantify the influence of clay and is given by

$$\frac{1}{R_t} = \frac{{\phi_t}^m\, {S_w}^n}{\alpha\, R_w} \left(1 + B\, Q_v\, \frac{R_w}{S_w}\right) \qquad (2)$$

where $\boldsymbol{B}$ is the equivalent counterion mobility (mho cm$^2$/meq) expressed as

$$B = \left[1 - 0.6 \exp\left(-0.77/R_w\right)\right] 4.6 \qquad (3)$$

and $\boldsymbol{Q_V}$ is the volumetric charge density (meq/mL) expressed by

$$Q_v = \rho_g\, \frac{1-\phi}{\phi}\, CEC \qquad (4)$$

where $\boldsymbol{\rho_g}$ is the grain density of the aquifer and $\boldsymbol{CEC}$ (meq/g) cation exchange capacity (Revil, 1998). For a mixture of clay minerals, the total $\boldsymbol{CEC}$ is given by

211 $$CEC = \varphi_W \sum X_i \, CEC_i \quad (5)$$

212 $\boldsymbol{X_i}$ is the relative fraction of each clay minerals in the fraction of the rock, $\boldsymbol{CEC_i}$ is the cation exchange
213 capacity of each of these clay minerals and $\boldsymbol{\varphi_w}$ is the mass fraction of clay in the rock.

214 Before applying these models, both formation and pore water resistivities must be normalized to a
215 temperature of 25°C, as temperature also influences electrical conductivity, and 25°C is the
216 temperature at which the water saturation equations were developed. The conversion is done using the
217 following equation (Arps, 1953):

218 $$R = R_F \left[\frac{T+21.5}{T_F+21.5}\right] \quad (6)$$

219 where $\boldsymbol{R}$ is the new resistivity calculated at the temperature desired (25°C), $\boldsymbol{R_F}$ resistivity at formation
220 temperature, $\boldsymbol{T}$ is the temperature desired (25°C) and $\boldsymbol{T_F}$ is the formation temperature (°C).

221

222 3.2. *Petrophysical model input data*

223 3.2.1. Structural-conceptual interpretation of ERT geophysical data

224 Geophysical data comprised an ERT profile of 1,305 m along a catchment hillslope transect crossing
225 the three borehole clusters locations (Fig. 1). The tomography was carried out using a Syscal Pro
226 resistivity meter with 60 electrodes distributed on 5 cables with a spacing of 5 meters, extending the
227 acquisition length by using the roll-along technique. Dipole-dipole (DD) and multi-gradient (mGD)
228 arrays were combined to optimize the resolution of geological structures (Comte et al., 2012b).
229 Measurement errors (standard deviation after stacking) higher than 4% were filtered out, in total 1.6%
230 of the pre-processed raw dataset. The average error for the remaining dataset was 0.13% with only
231 2.2% of the data having errors between 1% and 4%. Data inversion was implemented using
232 RES2DINV v3.58 (Geotomo Software) with a depth of investigation analysis (DOI) index of 0.1 as
233 proposed by Oldenburg and Li (1999). The overall inversion error was 9.6% and the model block
234 resistivity uncertainty ranged 1-21% with an average of 4% across the section. Further details of
235 acquisition and processing are in Comte et al. (2012a).

ERT inversion results revealed a subsurface layering with strong resistivity changes (Fig. 3a). Comte et al. (2012a) proposed a conceptual interpretation with low resistivities (< 500 ohm.m) representing the alluvium and clay-till sediments, fully saturated in their majority. A high resistivity zone (> 1,000 ohm.m) mainly characterized by unsaturated psammite schist with low clay content in the NNW zone of the study area. Below this layer, the resistivity increased ranging from 500-2500 ohm.m interpreted as the weathered/fissured schist. At the bottom of the profile, the most resistant zone (> 1000 ohm.m) is formed by unweathered mica schist with very low fracture density (Fig. 3b).

A refined interpretation was proposed in this case study. Using prior understandings (Moe et al., 2010; Comte et al., 2012a) of borehole and ERT data, a model comprised of five hydrogeological units has been used: (1) a deepest layer (massive bedrock, MB) of high resistivities (> 1,000 ohm.m) with low to null clay content and a low fracture density; (2) over the MB, the resistivities ranging from 500-3,000 ohm.m represents a weathered/fissured schist (fissured bedrock, FB) with higher clay content and the major thickness variability (5-30m); (3) the third layer (broken bedrock, BB) is characterized by high resistivities at high elevation (300-2,500 ohm.m) decreasing in SSE direction with an unsaturated zone and relatively low clay content (clay-leached horizon, Comte et al. 2019); (4) resistivities below 750 ohm.m are considered as the glacial deposit's unit, unsaturated in some areas and intercalated by the BB unit; (5) the alluvium is the fifth unit in this model, with presence only in the surrounding area of the GO3 borehole, it has the lowest resistivities (< 300 ohm.m) in the ERT profile (Fig. 3c).

### 3.2.2. Borehole logging analysis

The boreholes in the Gortinlieve catchment were drilled in three clusters (GO1, GO2, GO3). GO1 and GO2 have three wells, while GO3 has four wells to monitor the catchment at different hydrogeological units (Table 1). Logging analysis for this case study included gamma ray (GR) and temperature (T) logs.

262 **Table 1.** Borehole clusters of monitoring programme by Irish EPA. Modified from *Moe et al. (2010).*

| Monitoring Well | Depth (m) | Borehole completion | Uncased (open) Interval (m) | Zone | Elevation (m. a. s. l.) |
|---|---|---|---|---|---|
| GO1-Deep | 76.20 | Uncased 6 in. borehole | 46.60-76.20 | Massive bedrock | 174 |
| GO1-Shallow | 13.11 | Uncased 6 in. borehole | 4.72-13.11 | Fissured bedrock | |
| GO1-Transition | 2.44 | 6 in. PVC screen with 2mm slots, screen covered with 300-micron filter fabric | 0.65-2.20 | Broken bedrock | |
| GO2- Deep | 67.06 | Uncased 6 in. borehole | 29.26-67.06 | Massive bedrock | 88 |
| GO2-Shallow | 15.24 | Uncased 6 in. borehole | 7.92-15.24 | Fissured bedrock | |
| GO2-Transition | 3.05 | 6 in. PVC screen with 2mm slots, screen covered with 300-micron filter fabric | 0.63-2.85 | Broken bedrock | |
| GO3-Deep | 53.34 | Uncased 6 in. borehole | 36.27-53.34 | Massive bedrock | 33 |
| GO3-Shallow | 23.77 | Uncased 6 in. borehole | 12.19-23.77 | Fissured bedrock | |
| GO3-Transition | 7.15 | 6 in. PVC screen with 2mm slots, screen covered with 300-micron filter fabric | 4.73-6.95 | Broken bedrock | |
| GO3-Subsoil | 3.35 | 6 in. PVC screen with 2mm slots, screen covered with 300-micron filter fabric | 1.63-3.20 | Subsoil | |

263

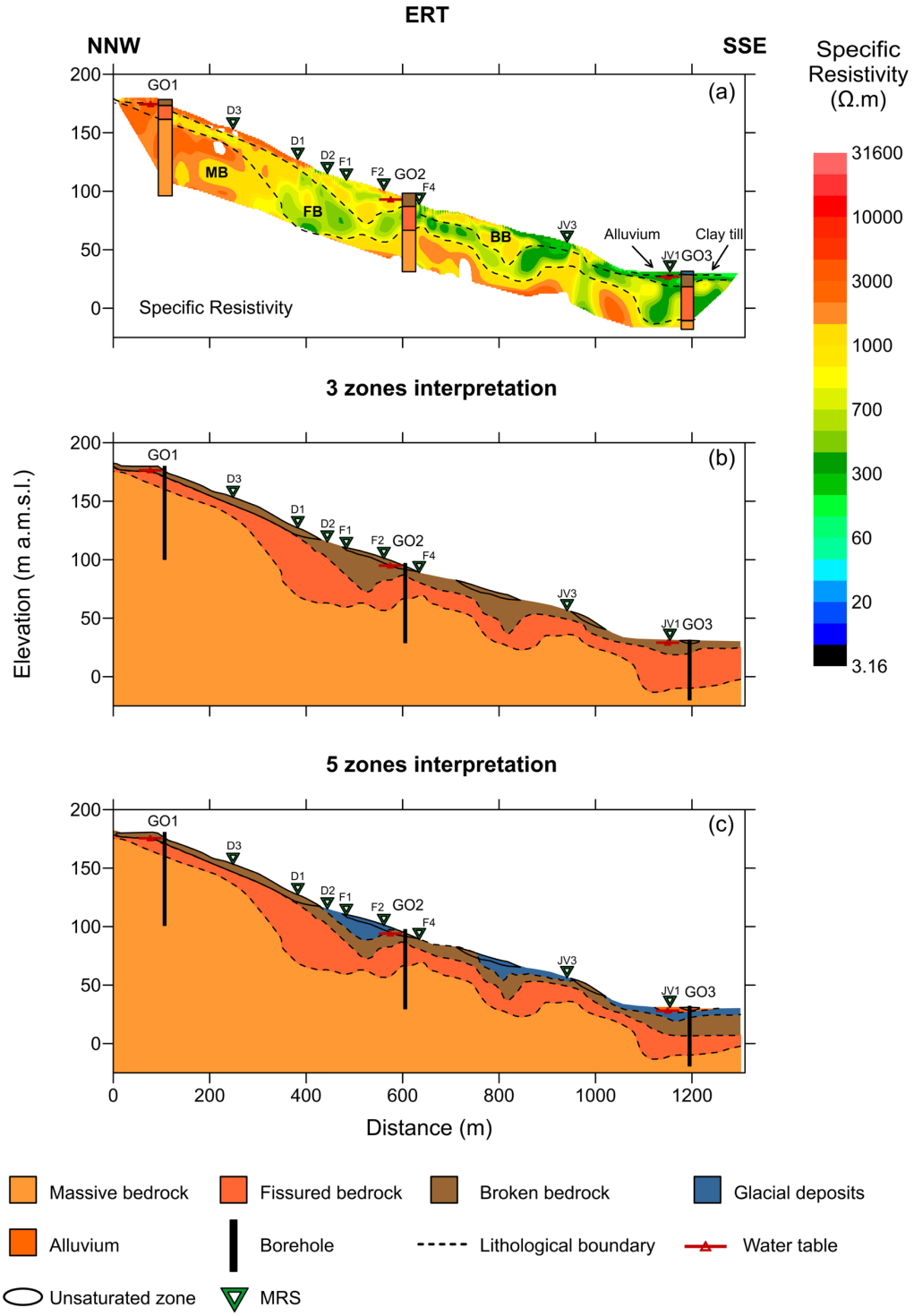


264

265 **Figure 3.** Inverse resistivity model of the Gortinlieve catchment along with two alternative

266 hydrogeological conceptual interpretations. GO1, GO2, GO3 indicate borehole locations and triangles

267 indicate locations of magnetic resonance soundings.

268

### 3.2.3. Characterization of clay minerals and electrical properties

The bedrock in this study area has a significant content of clay deposited in the fractures due to weathering processes in the aquifer (Caulfield et al., 2014) reducing the pore space. Clays are fined-grained high porosity minerals or soil material with a low hydraulic conductivity, so the water cannot easily flow through them (Moreno-Maroto and Alonso-Azcárate, 2018). For the application of the Waxman & Smits model, unlike Archie's model, the total CEC of the rock was required and computed using the Eq. (5) using (1) the nature (with known CEC ranges for individual minerals $\boldsymbol{CEC_i}$ are reported in Table 2) and respective proportions of clay minerals $\boldsymbol{X_i}$ for the site as reported from the analysis of borehole cuttings by Caulfield et al. (2014) and (2) total clay volumes, expressed a clay mass fraction in the bulk rock $\boldsymbol{\varphi_w}$, estimated using gamma ray (GR) logs.

The gamma ray log measures the natural radioactivity of a formation (expressed in API units) and it can be used to estimate the clay weight fraction. The gamma ray logs measure the radioactive material of the formations surrounding the borehole at a constant rate by measuring three primary isotopes Potassium (K), Thorium (T) and Uranium (U) which are highly concentrated in clay minerals. Therefore, GR logs mostly respond to parts of the rock formation matrix that is weathered into clays. Water circulation is a major factor for weathering, and since it is primarily controlled by fractures, it is expected that weathering clays predominantly occur in and in the vicinity of hydraulically active fracture (sometimes subsequently clogging fractures and hampering flow).

Clay weight fractions were obtained from GR by assuming two relations specifically for this case study. First, a linear relation expressed as

$$\varphi_w = I_{GR} = \frac{GR_{log} - GR_{min}}{GR_{max} - GR_{min}} \qquad (7)$$

where the $\boldsymbol{I_{GR}}$ is the gamma ray index, $\boldsymbol{GR_{log}}$ is the gamma ray log reading, $\boldsymbol{GR_{min}}$ is the minimum gamma ray value corresponding to a clean clay point (0%) and $\boldsymbol{GR_{max}}$ is the maximum gamma ray value in a saturated clay point (100%) according to pure clay values for the observed clay mineral as reported by Revil et al., (1998): Chlorite,180 API; Illite, 250 API; Montmorillonite, 150 API; Muscovite, 250 API. Second, a non-linear relation expressed as

295 $$\varphi_w = 0.33 \times (2^{2I_{GR}} - 1) \qquad (8)$$

296 that compensate for the different clay mineral proportions for shale (Revil et al., 1998; Ellis and
297 Singer, 2007). The gamma ray index ($I_{GR}$) was scaled into percentage to estimate the clay weight
298 fraction of the formations. Borehole analysis for clays (Caulfield et al. 2014) described constant clay
299 mineralogy across the study area, with variations in clay mineral relative proportions and clay weight
300 fractions according to the hydrogeological unit. Average values for clay weight fraction were
301 estimated from GR logs for each borehole and hydrogeological zone (Table 3). For detailed clay
302 volume analysis, see the supplementary material (S1).

303

304 **Table 2.** Cation exchange capacity (CEC) of the clay minerals present in the Gortinlieve catchment
305 (Dolcater et al., 1972; Meunier, 2005; Christidis, 2010; Bibi et al. 2016).

| Clay mineral | CEC (meq/100g) | Selected CEC (meq/100g)* |
|---|---|---|
| Chlorite | 10-40 | 20 |
| Illite | 10-40 | 20 |
| Montmorillonite | 80-120 | 90 |
| Muscovite | 1-10 | 1 |

306 * Distributed according to their clay mineral volume using method proposed by Revil et al. (1998).

307

308 The $I_{GR}$ yielded clay volumes with small variations between boreholes GO1 and GO2. In contrast, the
309 GO3 borehole had higher variations of clay volume decreasing from the BB to the FB. The major
310 impact of clay volume changes was observed when the CEC of each mineral was introduced in the
311 Waxman & Smits model, quantifying the variations in the total CEC values (Eq. 5). According to the
312 clay mineralogy, all three main bedrock hydrogeological units (BB, FB, MB) are dominated by
313 muscovite. Outside the FB in GO2, the most deeply weathered location, muscovite accounts for
314 between 40% and over 80% of all clay minerals. The FB unit has consistently the most balanced clay
315 mineralogy (in proportions of muscovite, chlorite, illite, and montmorillonite) and is simultaneously,

316 because of its highest proportions of illite and montmorillonite, the unit with the highest total CEC. In
317 contrast, the MB is devoid of both minerals due to insignificant weathering, while the BB has
318 relatively low proportions of these minerals, finally resulting in lower CECs than the FB for both
319 units. This distribution is interpreted as secondary clays produced by weathering of predominantly the
320 BB, and to a lesser extend the FB, being leached from BB and accumulate in fissures and fractures of
321 the FB unit. As this pattern in clay proportions is very consistent within each hydrogeological unit
322 (BB, FB, MB) we assumed that mineralogy and CEC, and their associated uncertainty, can reasonably
323 be interpolated across each unit along the whole 1300 m transect.

324

325 **Table 3.** Clay minerals identified in the groundwater monitoring wells. Gamma ray mean value per
326 zone using linear and non-linear relation. Clay weight fraction and total CEC per zone. Modified from
327 *Comte et al. (2019).*

| | **Chlorite (%)** | **Illite (%)** | **Montmorillonite (%)** | **Muscovite (%)** | **Natural gamma (cps)** | **Clay weight fraction (%)** | **Total CEC (meq/100g)** |
|---|---|---|---|---|---|---|---|
| GO1 | | | | | | | |
| Broken bedrock (BB) | 26.8 | 7.5 | 7.9 | 57.9 | 116 | 49.7 | 5.9 |
| Fissured bedrock (FB) | 20.2 | 21.7 | 18.1 | 40.0 | 111 | 48.6 | 11.2 |
| Massive bedrock (MB) | 34.2 | 0.0 | 0.0 | 65.8 | 102 | 42.6 | 1.7 |
| GO2 | | | | | | | |
| Broken bedrock (BB) | 11.5 | 8.4 | 4.8 | 75.4 | 101 | 40.1 | 3.1 |
| Fissured bedrock (FB) | 3.3 | 46.7 | 31.9 | 18.0 | 102 | 44.7 | 17.3 |
| Massive bedrock (MB) | 17.5 | 0.0 | 0.0 | 82.5 | 116 | 46.6 | 1.2 |
| GO3 | | | | | | | |
| Alluvium | 13.5 | 5.4 | 3.9 | 77.2 | 40 | 13.3 | 0.9 |
| Glacial till | 13.5 | 5.4 | 3.9 | 77.2 | 45 | 15.5 | 1.1 |
| Broken bedrock (BB) | 13.5 | 5.4 | 3.9 | 77.2 | 78 | 30.0 | 2.0 |
| Fissured bedrock (FB) | 5.5 | 39.6 | 26.6 | 28.3 | 41 | 14.8 | 4.8 |
| Massive bedrock (MB) | 17.5 | 0.0 | 0.0 | 82.5 | 116 | 46.6 | 1.2 |

328

329 3.2.4. Other input parameters for the Archie and W&S models

330 Not all the input parameters for the petrophysical models were available from the study site: this
331 includes the rock density, porous media tortuosity, and cementation exponent which are empirical
332 parameters that have been constrained from previously published literature (Table 4). The
333 cementation exponent (*m*) is the most important parameter in Archie's law, depending on the porosity
334 and fracture density (Archie, 1942; Aguilera, 1976). These authors found a relationship between the
335 pore connectivity and the fracture network stating that high fracture content is associated with a low
336 cementation exponent (Aguilera, 1976). Other authors suggested that the shape of the grains and the
337 pores are more significant for variations of the cementation exponent than other properties (Salem and
338 Chilingarian, 1999). More recent studies claimed that *m* is dependent on the connectedness (transport
339 pathways), taking into account its variation as a function of porosity and the connectivity of the
340 matrix. The connectedness, also known as conductivity formation factor, describes how the electrical
341 conductivity of a fluid is modified by the presence of solid non-conducting grains. (Glover, 2009,
342 2010).

343 Additionally, the studied hard rock aquifer had a significant volume of clay, which can lead to an
344 increase of *m* depending on the volume and type of the clay (Waxman & Smits, 1968; Salem and
345 Chilingarian, 1999). As a conclusion, the cementation exponent is not easy to determine because is
346 highly affected by several factors. However, previous studies (Salem, 2001; Tabibi and Emadi, 2013;
347 Kazakis et al., 2016) have proposed *m* values for weathered/fractured aquifers with clay content to
348 predict reservoir quality and performance. In this work, *m* was calibrated using the range of values
349 provided by these studies (Table 4).

350 An average density range was calculated for each hydrogeological unit according to the rock types
351 identified in the borehole cuttings. The third of these parameters was the tortuosity ($\alpha$), defined as a
352 ratio of fluid flow in a porous media (Pisani, 2011; Tokan-Lawal et al., 2014). For this study, the
353 value of $\alpha$ was fixed at 1.4 (Urish, 1981; Aguilera, 2008; Piedrahita and Aguilera, 2017) for all the

354 hydrogeological units due to its low impact in zones with low porosity, a primary characteristic of this
355 catchment.

356

357 **Table 4.** Parameters used to quantify porosity for Archie and Waxman & Smits model. Modified from
358 *Comte et al. (2019)*

| | **Water temperature (°C)** | **Cementation exponent[a]** | **Rock density ($g/cm^3$)[b]** | **Water resistivity (Ω.m)** |
|---|---|---|---|---|
| Alluvium | 15.5-16.0 | 1.8 | 1.50-2.20 | 22.22-22.65 |
| Glacial till | 13.5-16.0 | 2.05 | 1.60-2.0 | 22.22-29.63 |
| Broken bedrock | 12.1-16.0 | 2.5 | 2.45-2.55 | 22.22-37.04 |
| Fissured bedrock | 12.8-14.2 | 2.0 | 2.6-2.70 | 20.0-34.48 |
| Massive bedrock | 12.7-13.1 | 1.5 | 2.75-2.85 | 17.54-30.03 |

359 [a]Cementation exponent (Salem, 2001; Tabibi and Emadi, 2013; Kazakis et al., 2016)

360 [b]Rock density (Sharma, 1997; Caulfield et al., 2014; Schön, 2015)

361

362 The Archie and Waxman & Smits models were applied considering different saturation values ($S_w$) in
363 the aquifer unsaturated zone. Both models were quantified using 4 percentages of saturation (100%,
364 75%, 50%, and 25%) introduced in the respective equations (Eq. 1,2). The unsaturated zone was
365 structurally delineated from ERT as representing a thin shallow layer of up to a few meters depending
366 on the location.

367

368 3.3. *Spatial interpolation of borehole-based petrophysical parameters*

369 Considering that some of the input data for the petrophysical models were only available at 3 borehole
370 locations, these parameters were spatially interpolated and extrapolated to provide 2D spatial
371 distributions over the same grid as the input ERT data. Interpolation was performed following three
372 conceptual-structural scenarios; (1) simple (unconstrained) interpolation, (2) structurally constrained

interpolation using 3 conceptual hydrogeological units based on the ERT interpretation and (3) constrained using 5 conceptual units based on the ERT interpretation. The process was carried out using SURFER v13.0 by Golden Software considering three interpolations methods; nearest neighbor, triangular interpolation, and kriging.

Borehole parameters included in the interpolation process were water temperature ($T$), water resistivity ($R_w$), cementation exponent ($m$), rock density ($\rho$), and cation exchange capacity ($CEC$). The nearest-neighbor method was finally chosen for subsequent work as being less subject to artifacts than the other two methods.

### 3.4. *Sensitivity and uncertainty analysis*

Sensitivity analysis (SA) aimed at exploring the robustness and accuracy of model results for either Archie or Waxman & Smits by understanding the impact of the variations in individual input parameters on the outputs of the model (Balaman, 2019). The SA measured the impact of change in the model by introducing increments or decrements of ±15% and ±30% in the parameters and quantifying the percentage change of each of them. This enabled us to distinguish between high-leverage parameters, whose values have a significant impact on the model behavior and low-leverage parameters, whose value have minimal impact in the outputs (Jørgensen and Fath, 2011), and focus on the significant parameters to reduce uncertainty and increase the reliability of the model due to the high sensitivity of Archie's and Waxman & Smits.

Uncertainty analysis (UA) was further carried out to quantify the variability of the final model output that is due to the combined variability of all input parameters, which is considerable in a large-scale study. The following workflow was applied: (1) identify the model input parameters subject to uncertainty ($\alpha$ and $R_w$ are fixed values for maximum and minimum models; ERT measurement errors of 0.13% in average were disregarded as negligible compared to the subsequent resistivity inversion error of 9.6%, and the average resistivity model block error of 4%, see section 3.2.1); (2) quantify the variations (uncertainty) of all input parameters, in this case, according to hydrogeological conditions;

399 (3) generate maximum and minimum values of each parameter; (4) compute the maximum and
400 minimum model outputs; and (5) calculate the relative uncertainty (Geffray et al., 2019).

401 In this work, all input parameter errors were evaluated with minimum and maximum values according
402 to hydrogeological conditions (Table 5). This provided quantification of the relative uncertainty for
403 each parameter, and the petrophysical models in a 2D distribution. Additionally, the average relative
404 uncertainty per zone was obtained for Archie's and Waxman & Smits models, as in Eq. 9:

405 $$RU = \frac{AU}{MM} \times 100\% \qquad (9)$$

406 where RU is the relative uncertainty, AU is the absolute uncertainty and MM is the magnitude of
407 measurement.

408

409 **Table 5.** Parameters considered for uncertainty analysis with ranges of values and relative
410 uncertainties across the three hydrogeological units.

| **Parameter** | **Full range of values** | **Min-Max Rel. uncertainty (%)** |
|---|---|---|
| Cementation exponent (*m*) | 1.4 - 2.6 | 4 – 7 |
| Total CEC (meq/100g) | 1.10 - 30.03 | 49 – 150 |
| Density (g/cm$^3$) | 2.35 - 2.90 | 2.6 - 3.0 |
| Formation resistivity ($R_t$) (Ω.m) | 125 – 39,301 | 1 – 21 |
| Saturation water ($S_w$) | 0.25 - 1 | 0 - 75 |

411

412 3.5. *Model verification using water storage estimates from 1D magnetic resonance sounding*

413 For our study, we used NUMIS$^{plus}$ and NUMIS$^{poly}$ MRS equipments manufactured by IRIS
414 instruments (France). In Gortinlieve catchment, 11 MRS stations were located along the ERT profile
415 with three stations situated as close as possible to the boreholes (Fig. 1). Three of them were rejected
416 because of low signal-to-noise ratio (SNR) and the remaining 8 MRS measurements were used in this
417 study (Comte et al., 2019). SAMOVAR software package was used to run one-dimensional inversion

418 of MRS data. See Legchenko et al. (2017) for a detailed description of processing and inversion of
419 MRS data. Accuracy of MRS results depends on the SNR defined by the ambient electromagnetic
420 noise, the target location relative to the measuring loop, and the amount of water in the subsurface
421 (Legchenko et al., 2011). The study area is characterized by a low porosity aquifer and the third
422 condition caused the major effect in the data quality. In general, MRS resolution and sensitivity
423 degrade with the increasing depth to investigated aquifer formation, which limits the depth of
424 investigation with MRS.

425

426 3.6. *Model comparison with pumping and recovery test*

427 Pumping and recovery tests were previously carried out by Comte et al. (2012a) in each borehole of
428 the study site and further interpreted to provide values of transmissivity, hydraulic conductivity, and
429 storativity (see Comte et al., 2012a, for acquisition methodology and interpretation results). These
430 values, especially storativity, would be representative of a very small volume around the open
431 boreholes due to the low pumping rate possible in such low productivity aquifer, and more so for the
432 deep boreholes. As a result, values could be affected by small scale heterogeneities (e.g. preferential
433 flow pathways) and possibly locally enhanced fracturing associate to the downhole hammer drilling
434 process as well as washing of clay clogging in existing fractures due to drilling fluids. To limit the
435 influence of small scale heterogeneities, the storativity values in each bedrock zone intersected by the
436 boreholes (BB, FB, MB), were averaged to provide one value per zone (Table 6). Average storativity
437 values were then compared to corresponding average values of ERT-derived porosity (Archie and
438 Waxman & Smits) and MRS-derived water content for each zone.

439

440

441

442

443

444 **Table 6.** Storativity values per zone (from Comte et al., 2012a)

| Zone | Storativity average (-) | Min | Max | Data points |
|---|---|---|---|---|
| Broken bedrock (BB) | 0.05 | 0.05 | 0.05 | 2 |
| Fissured bedrock (FB) | 0.01 | 0.001 | 0.02 | 3 |
| Massive bedrock (MB) | 0.005 | 0.005 | 0.005 | 2 |

445

446 **4. Results**

447 4.1. *Spatial distribution of input parameters for petrophysical models*

448 The results of interpolating all the petrophysical model input parameters using the nearest neighbor
449 algorithm (Fig. 4) matched overall the constraints (input data values) at the borehole locations.
450 However, the use of a non-structurally constrained interpolation developed artifacts in the data
451 distribution producing unrealistic geological structures. In detail, *CEC* spatial patterns exhibited a
452 compartmentalized tabular distribution, with strong lateral and vertical changes. The tabularity angle
453 was controlled by the value applied in the search limits (6.5° taken as the average topographical
454 slope). Similar behavior was found in the other parameters ($m$, $R_w$, T, ρ) with a lower degree of
455 change in all directions due to the low variability of the initial data for the model without structural
456 constraints.

457 The two structurally-constrained interpolations (with 3 and 5 zones, respectively) produced more
458 realistic parameter distributions. Both structurally-constrained interpolations had similar outputs in the
459 upper 1000 m of the modeled profile, slightly differing in the lower 500 m beneath the valley flat. In
460 general, the 5 structural unit model distribution suffered a ´pull-up´ of the data in the vertical direction
461 over 500 m. Comparing the models of 5 and 3 zones, the 5 zones model suffered a decrease in values
462 for *CEC*, $m$, and $R_w$ in the MB and FB while an increase for $T$ and $\rho$ in the MB and FB in the
463 surrounding area near the GO3 borehole. *CEC* interpolation yielded a distribution highly influenced
464 by the hydrogeological units' model, having the highest values (> 0.11 meq/g) in the FB specifically

in the center zone of the aquifer. In the case of *m,* the difference between the two structurally-constrained interpolations demonstrated that the major impact occurs in the last 500 m of the modeled profile, keeping a smooth lateral and vertical distribution of the data that perfectly delineates the two hydrogeological conceptual models.

Interpolation of rock density, with a low variation (2.4-2.9 g/cm$^3$) for the rock minerals encountered in the study area produced similar patterns as *m*, having a distribution with smooth vertical and lateral changes. $R_w$ and *T* interpolation exhibited significantly different spatial patterns than other parameters, with large variability and relative compartmentalization in lateral directions with minor influence of the structural constraints in the interpolations. This is due to these hydrogeological parameters ($R_w$ and *T*) having much larger lateral (upslope-downslope) variability than vertical (depth) variability. Interpolated ranges of values for these parameters are within the input data limits ($R_w$ = 18-36 ohm.m; T = 12-16°C).

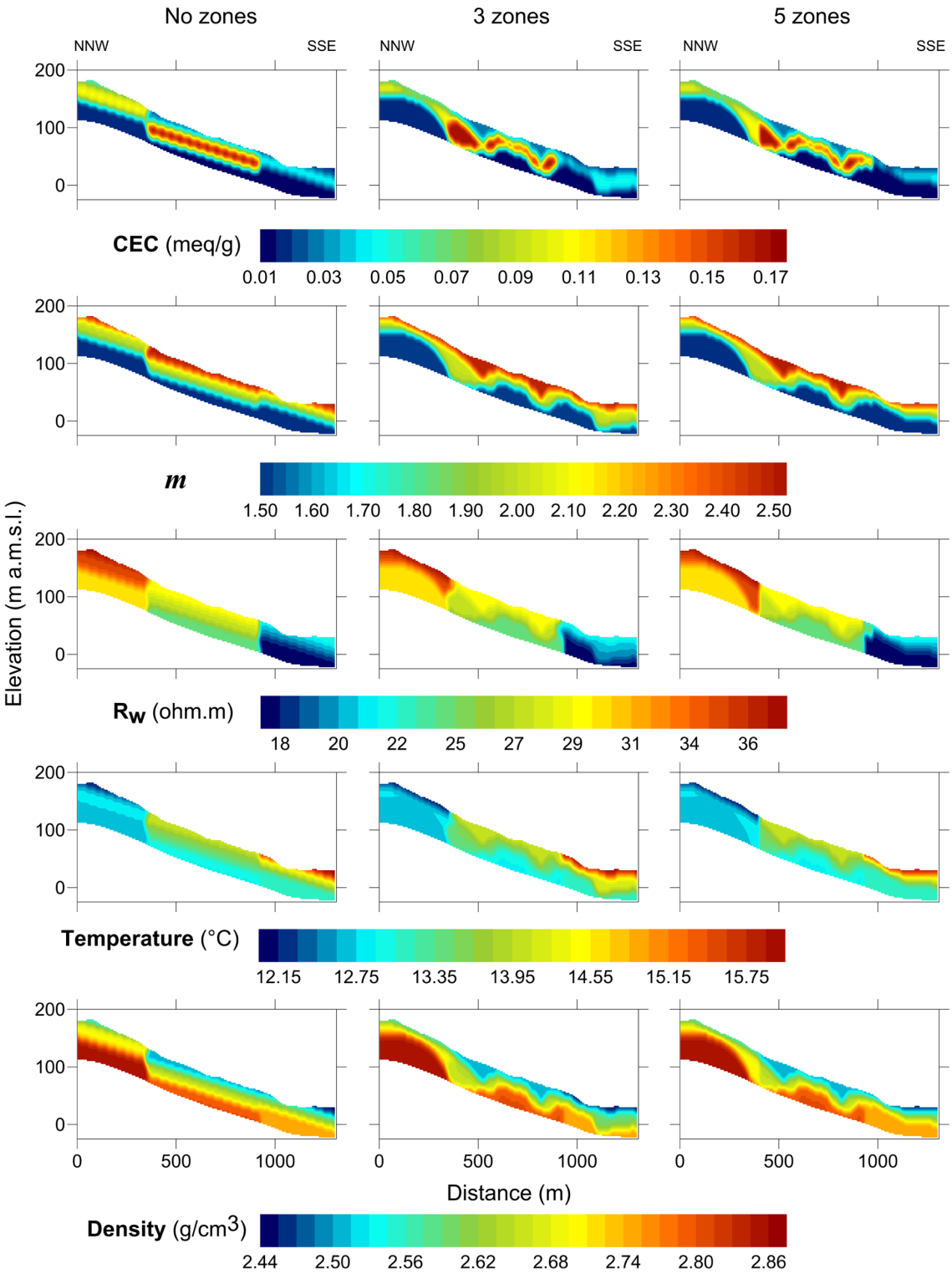


**Figure 4.** Nearest neighbor interpolation results of borehole-based petrophysical parameters; cation exchange capacity (CEC); cementation exponent (m); water resistivity ($R_w$); temperature (T) and rock density (ρ); without (single unit) and with (3 units and 5 units) structural constraints based on conceptual interpretation of resistivity model.

### 4.2. *Porosity predictions*

The 2D porosity models resulting from computing the 2D inverted ERT data (Fig. 3a) and the 2D interpolated parameter distribution (Fig. 4) in the two selected petrophysical models (Archie and Waxman & Smits) are presented in Fig. 5. As expected, the conceptual constraints used when interpolating the petrophysical input parameters had a major influence on the final spatial distribution of porosities. The porosity distribution obtained with no conceptual constraints exhibits tabular layering of massive, fissured, and broken bedrock. Uphill, porosities were an order of magnitude lower than in the mid-slope and downslope areas, with abrupt changes in porosities. A distribution that did not match well the initial structural interpretation of the resistivity profile.

Distributions using 3 and 5-zone structural constraints showed spatial patterns of porosity that better match the original ERT interpretation and associated conceptual model. Highest porosity values were found in the shallow (broken) bedrock characterized by lower resistivities. The deep and intermediate zones (MB and FB) had the lowest values of porosity associated with fracture density and aperture as well as weathering intensity (secondary clay content) decreasing with depth. The downslope area, nearby GO3 borehole, exhibited the highest porosity values of all three conceptual models, with a vertical distribution largely controlled by the applied structural constraints. The generally lower porosities obtained uphill for all models were consistent with the different, less weathering-prone psammite lithology as evidenced from outcrop observation and ERT result showing thinner broken and fissured horizons.

Archie's model overall produced porosity values ranging between $3 \times 10^{-2}$ (i.e. 3%) to $7 \times 10^{-1}$ (i.e. 70%) for the three conceptual models with arithmetic mean values of 16% (no zones), 17% (3 zones) and 16.5% (5 zones). The 3-layer model (3 hydrogeological units) was considered as the best model. Although both 3-layer and 5-layer models well preserved the geological structure, the alluvium and glacial deposits which were additionally considered in the 5-layer model (Fig. 3), remained zones of small volume having very little impact in the final porosity models. Therefore the 3-layer model appeared as best to compromise in terms of resolution and simplicity of parametrization and associated computational efficiency. In this model, the MB (massive unweathered and poorly

509 fractured mica schist) had the lowest average porosity (8 x $10^{-2}$, i.e. 8%) of the 3 units followed by an
510 increase of porosity in the FB (2 x $10^{-1}$, i.e. 20%) characterized by a weathered/fractured bedrock. At
511 the top, the BB reached the highest porosity (3 x $10^{-1}$, i.e. 30%) considering the glacial deposits and
512 alluvium units as the areas with the higher values. The Waxman & Smits porosity model produced
513 lower porosities than Archie's model by an order of magnitude with values for the non-structurally-
514 constrained model of 9 x $10^{-3}$ (i.e. 0.9%), and for the structural-constrained models of 1.3 x $10^{-2}$ i.e.
515 1.3% (3 zones) and 1.1 x $10^{-2}$ i.e. 1.1% (5 zones) in average. Waxman & Smits porosities rapidly
516 decreased with depth dropping from BB (5 x $10^{-2}$, i.e. 5%) by two orders of magnitude at the MB (3 x
517 $10^{-4}$, i.e. 0.03%) in terms of average porosity. The unsaturated zone considered 50% for water
518 saturation ($S_w$), increasing the porosities in the BB for both models (Archie and Waxman & Smits),
519 this applied for the 3 scenarios (1 non-structural and 2 structural-constrained). The unsaturated zone
520 was tested applying four alternative saturations ($S_w$ = 25%, 50%, 75%, and 100%) producing an
521 inverse relationship between $\phi$ and $S_w$. Archie´s model showed less dispersion of porosity values
522 showing a normal distribution within and across all the zones including the unsaturated area.
523 Contrastingly, the Waxman & Smits model had a higher spreading of the calculated porosity with a
524 log-normal distribution across, and a normal distribution within, each of the three zones (BB, FB, and
525 MB) (Fig. 6).

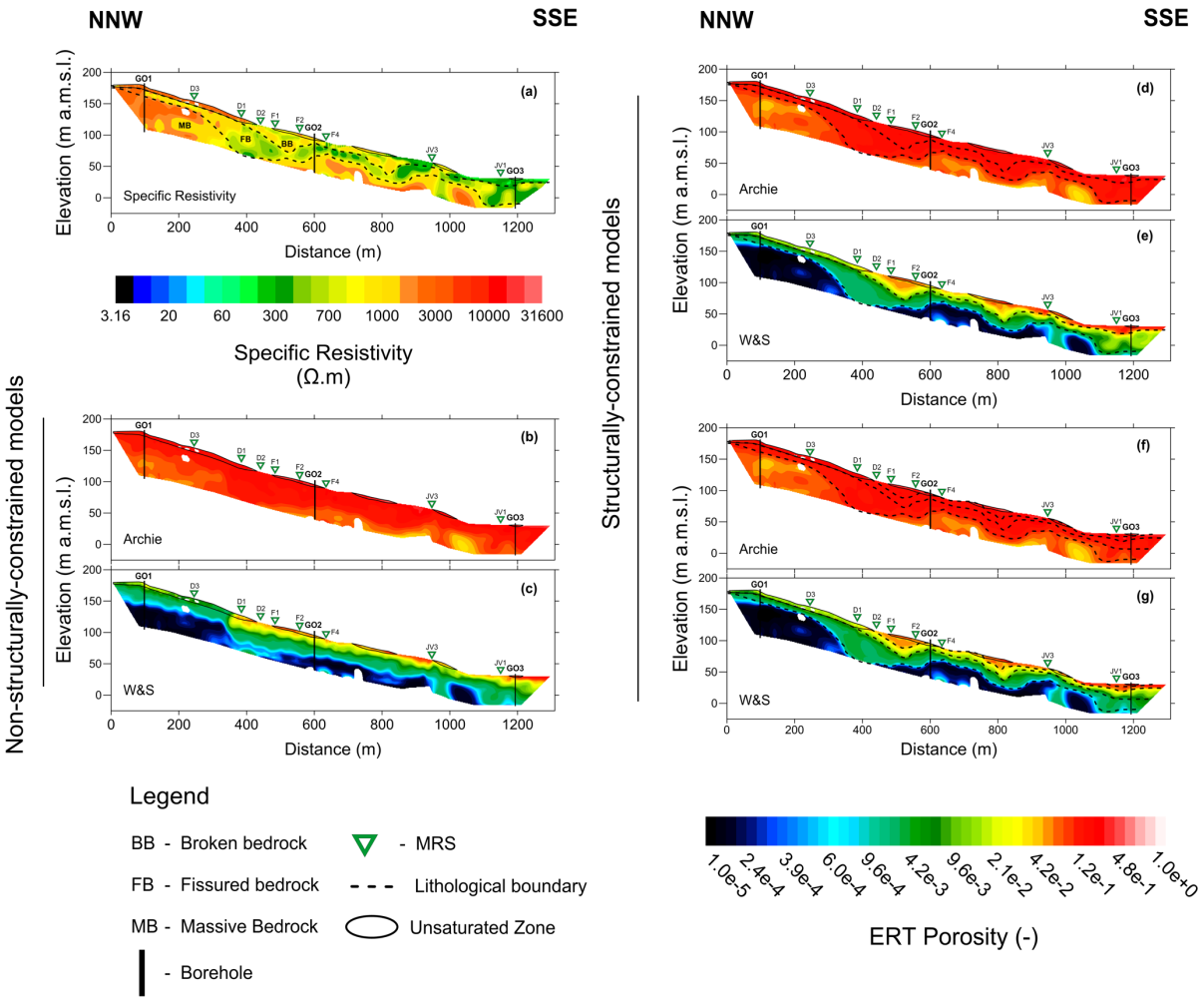


**Figure 5.** Predicted 2D spatial variations of porosity compared to original resistivity data. (a) original (input) inverted ERT profile. (b-g) predicted porosity distributions for different structural constraints and petrophysical models: Archie's model (b) and Waxman & Smits model (c) no structural constraint; Archie's model (d) and Waxman & Smits model (e) with 3 structural units; Archie's model (f) and Waxman & Smits model (g) with 5 structural units. Triangles at the ground surface indicate the location of MRS soundings (see section 3.5).

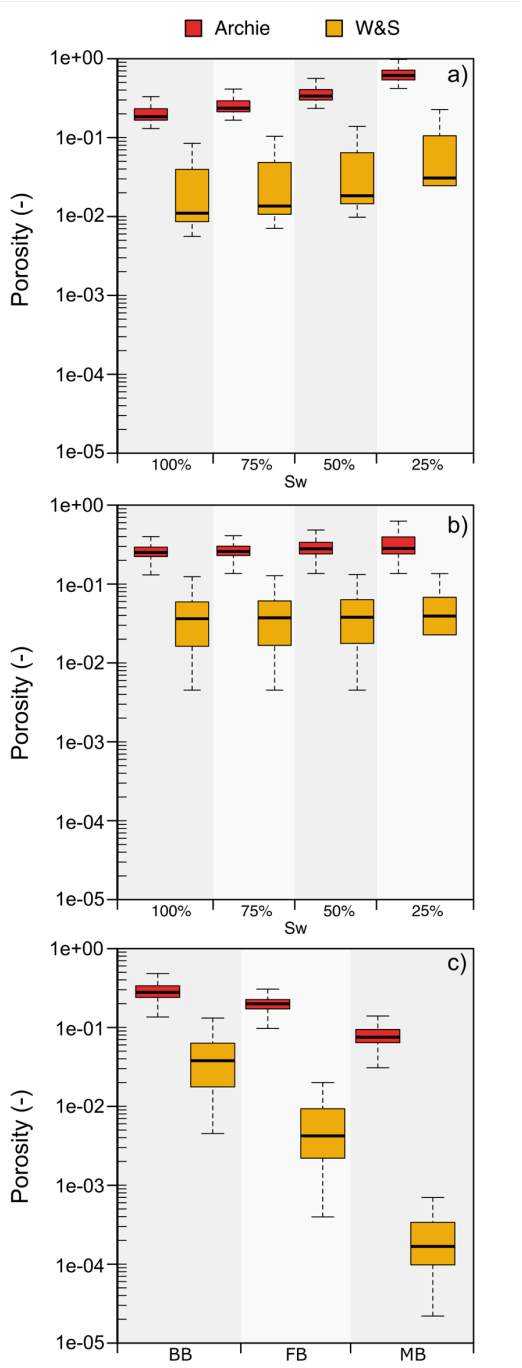


**Figure 6.** Porosity distribution per hydrogeological unit from Archie and Waxman & Smits model. (a) broken bedrock unsaturated zone considering 4 saturation values ($S_w$) 25, 50, 75 and 100%, (b) entire saturated and unsaturated broken bedrock unit and considering 4 values of saturation ($S_w$) above the water table, and c) three hydrogeological conceptual units BB, FB and MB (considering uniform 50% saturation water for the unsaturated zone.

### 4.3. *Sensitivity and uncertainty analysis*

The sensitivity analysis enabled us to quantify the weight of the petrophysical parameters involved in the forward modelling (Fig. 7). When using both Archie and Waxman & Smits models, the cementation exponent (*m*) appeared as the parameter responsible for the largest sensitivity. For the Archie model, a variation of ±15% produced porosity changes of ±26%. The Waxman & Smits model was even more sensitive to *m*, i.e. for the same ±15% of variation, porosity changed by 120% and -68% respectively. Saturation ($S_W$) was the second most sensitive parameter (18% in a 15% increment) in Archie´s model close to that of the *m* parameter while in the Waxman & Smits model the sensitivity to other parameters was not as high as for *m* but added together, they introduced significant uncertainty into the models.

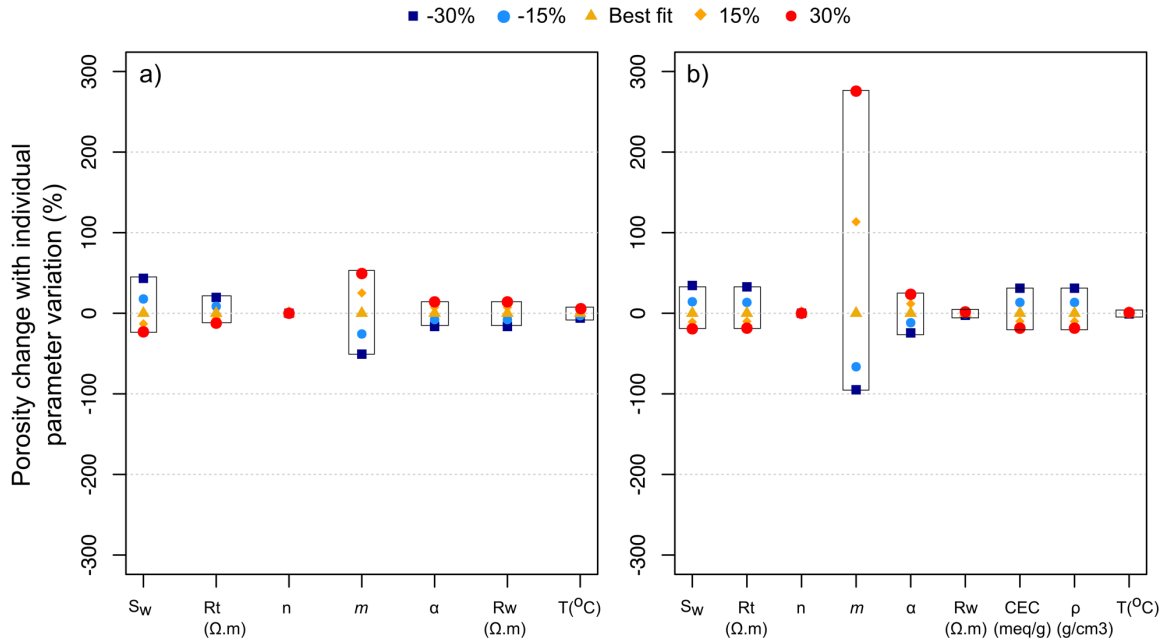


**Figure 7.** Sensitivity analysis of (a) Archie and (b) Waxman & Smits porosity models.

The uncertainty analysis provided valuable information with regards to the models´ accuracy. In this paper, we present the relative uncertainty computed for the model with 3 hydrogeological units using the maximum and minimum possible values for each input parameter as estimated from the geological

556 characteristics of the study area (Table 5). The final porosity predictions for Archie and Waxman &
557 Smits held relative uncertainties in predicted porosities of ±16% and ±105% (Fig. 8) and absolute
558 uncertainties of ±3 and ±1 on average, respectively. When looking separately at average uncertainties
559 for each specific hydrogeological conceptual unit (BB, FB, MB), MB had the lowest absolute porosity
560 uncertainty (where porosity is expressed in %) in both models (Archie = 1.44% and W&S = 0.06%)
561 decreasing with depth (Fig. 9a). In terms of relative uncertainty, the BB unit appeared as the zone
562 with the highest values in Archie's model (22% on average) while in Waxman & Smits the highest
563 relative uncertainty affected the MB, amounting 180% on average and 300% locally (Fig. 9b) i.e.
564 three times the best predicted values.

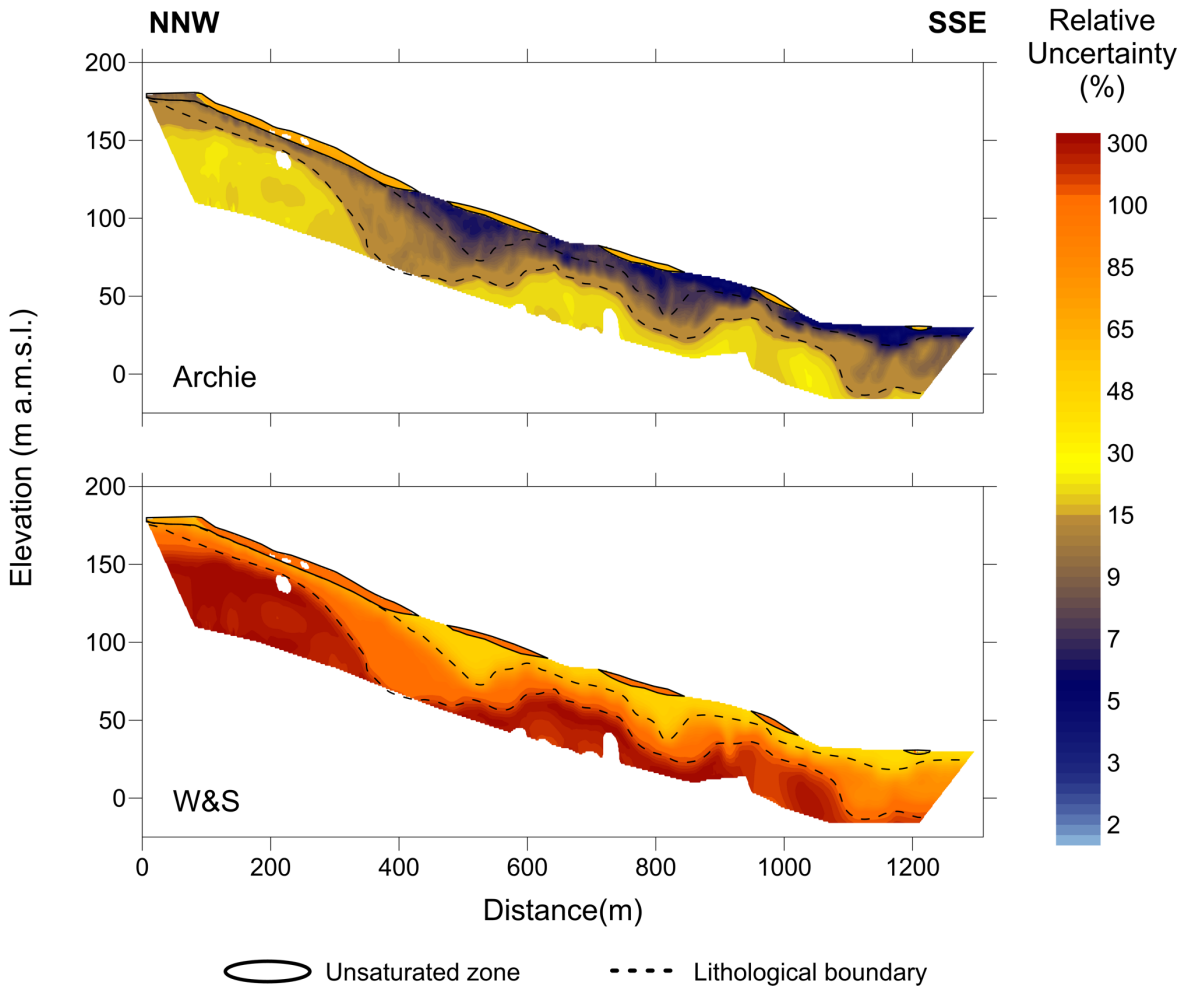


565

566 **Figure 8.** 2D relative uncertainty of Archie and Waxman & Smits porosity models.

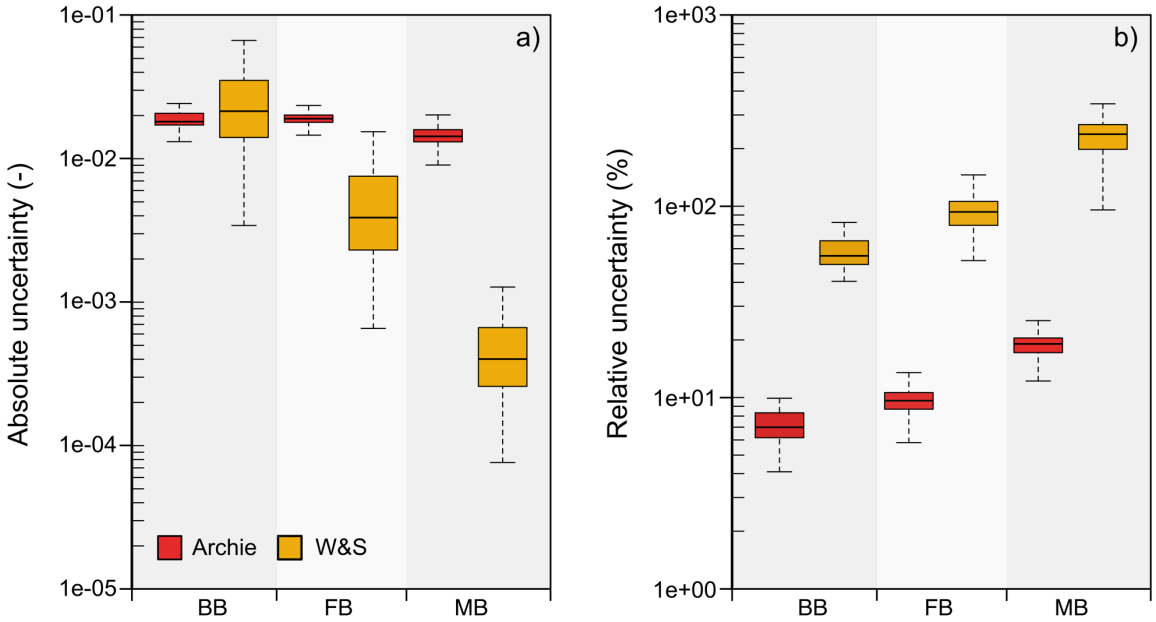


567

568 **Figure 9.** Box plots of (a) absolute and (b) relative porosity uncertainty per conceptual unit for Archie
569 and Waxman & Smits models.

570

571 The highest contributing factor to porosity uncertainty for the Archie model was the water saturation
572 (75% on average) while for the Waxman & Smits model the CEC (87% on average) had the highest
573 contribution (Fig. 10). While the water saturation also contributed to the uncertainty in W&S, the
574 influence was smaller compared to the uncertainty introduced by the CEC. Despite being the most
575 sensitive parameter in the model, the cementation exponent (4-7%) did not produce as high relative
576 uncertainty as the CEC did. In addition to the other parameter uncertainties, the formation resistivity
577 ($R_t$) obtained from ERT data inversion had a relatively low uncertainty (1-21%) and as such did not
578 impact significantly the final model uncertainty. Note that the uncertainty in the formation resistivity
579 only considers the ERT inversion errors but not the ERT measurement errors.

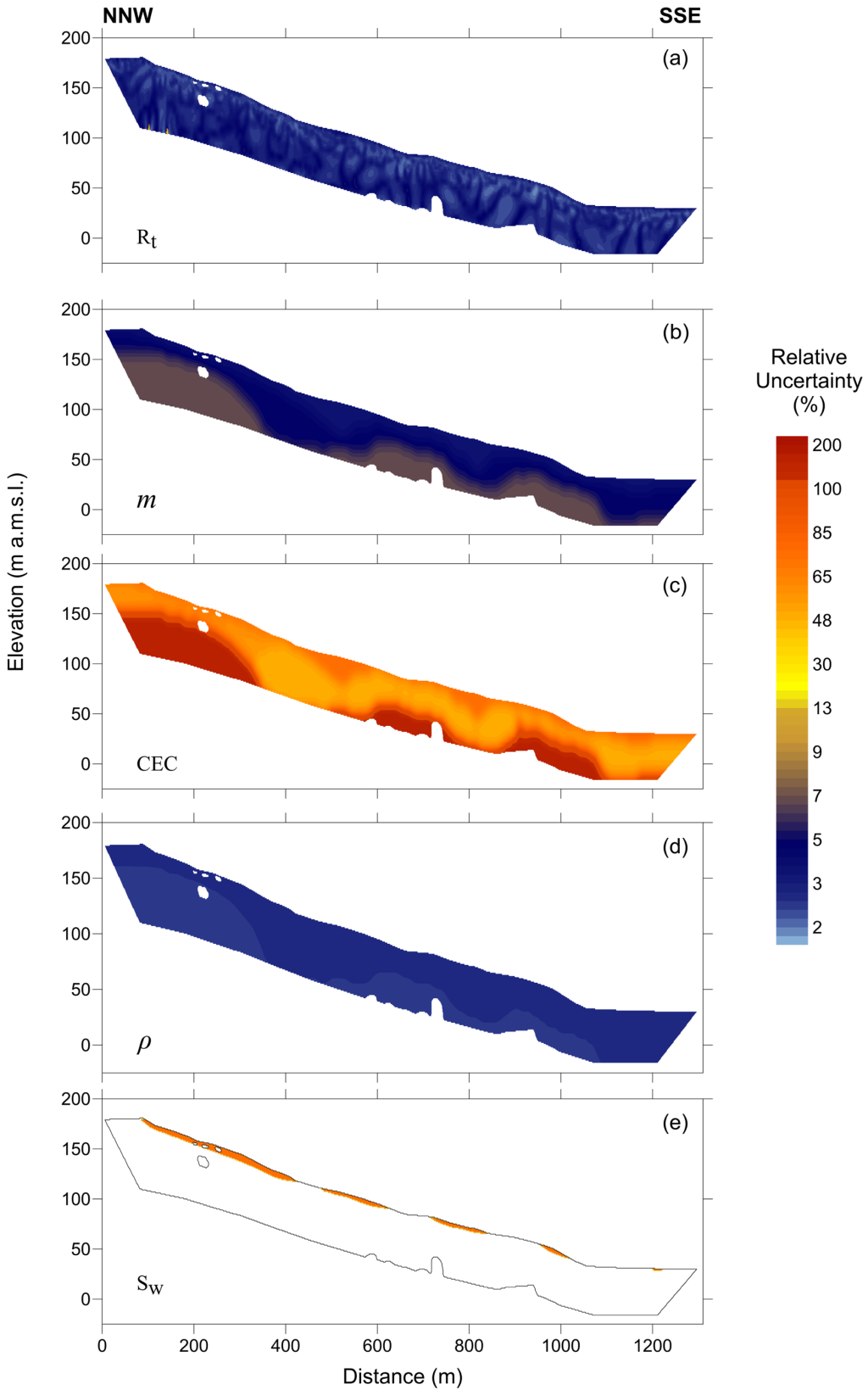


580

581 **Figure 10.** Uncertainty analysis of petrophysical models input parameters: formation resistivity ($R_t$),

582 cementation exponent (m), cation exchange capacity (CEC), rock density (ρ), and water saturation

583 ($S_w$).

584 In this study, the ERT measurements errors (standard deviation of 0.13% on average) were discarded
585 from the uncertainty analysis due to being negligible compared to the inversion error (9.6%) and
586 model block resistivity errors (4% on average). The very stable, low noise, measurement conditions
587 were to be attributed to excellent electrode coupling due to the favorable soil conditions (wet, clay-silt
588 soils and unsaturated zone), high water table and low anthropogenic noise. In different conditions,
589 such as drier/more resistant soils (e.g. in more arid regions), deep water table, or presence of
590 anthropogenic noise such as metal pipes, buried fences, etc. the ERT measurements would be less
591 stable with higher errors, which may need to be taken into account in the uncertainty analysis as the
592 would significantly increase the uncertainty in porosity estimates.

593

594 4.4. *Model verification using independent 1D water content data*

595 At each station, inversion of MRS measurements showed a vertical profile of the water content. The
596 water content was compared with the boundaries of hydrogeological units identified using the ERT
597 interpretation. It allowed to develop a correspondence between the water content value and the
598 geological formation. Thus, the average water content (WC) was estimated with MRS as 1% in the
599 massive bedrock, 2-3% in the fissured bedrock and in the broken bedrock ranging from 5 to 6%. In
600 the selected 8 MRS measurements, the highest WC was found in the profile F1 (1-6%) at 480m
601 NNW-SSE direction, characterized by a thick FB highly fractured and fully saturated. The lowest WC
602 (<2%) was shared by the profiles D1 and D3, at 240m NNE-SSW direction, located in a high
603 resistivity zone (MB) with low fracture density.

604 The water content profiles from MRS surveys were compared with the ERT porosity models (Archie
605 and Waxman & Smits) extracting the data in the nearest location to each MRS survey and presented
606 in the logarithmic scale (Fig. 11). Fig. 11 also shows the minimum and maximum models of the MRS
607 water content and the ERT porosity models. Archie porosity values were distinguished by largely
608 overestimating the pore space with values ranging 5-35 x $10^{-2}$ (5-35%) i.e. about an order of
609 magnitude (i.e. ~1000%) higher than water content obtained from MRS surveys for the broken and

fissured bedrock at all locations but decreasing with depth as expected for the study area. Massive bedrock estimates showed porosities ranging 1-1.5 x $10^{-1}$ (i.e. 10-15%), range rather expected for the broken bedrock. Not accounting for the clay content in the aquifer by using Archie´s law overestimated the porosity of the study area where typical porosities for this geological setting were widely reported are much lower (metamorphic rocks $\phi$ = ~ 4%) (Earle, 2015). Waxman & Smits porosity values had a slightly better fit with MRS water content data producing consistent spatial patterns at three locations. The best match occurred specifically in the profiles F1, F2, and JV1, locations where the minimum and maximum values for water content and ERT-derived porosities predicted the highest porosities (2-6 x $10^{-2}$). In the other 5 soundings, there were significant discrepancies between ERT-porosities and MRS water contents. The ERT porosity values from Waxman & Smits were higher than MRS water contents in the broken bedrock (0-10m) but lower in fissured and massive bedrock, overall providing lower groundwater storage values at higher depths. The clay content variations in the fissured and the massive bedrock could be a reason for this behavior but also the uncertainty attributed to this method (Waxman & Smits model) that increases with depth.

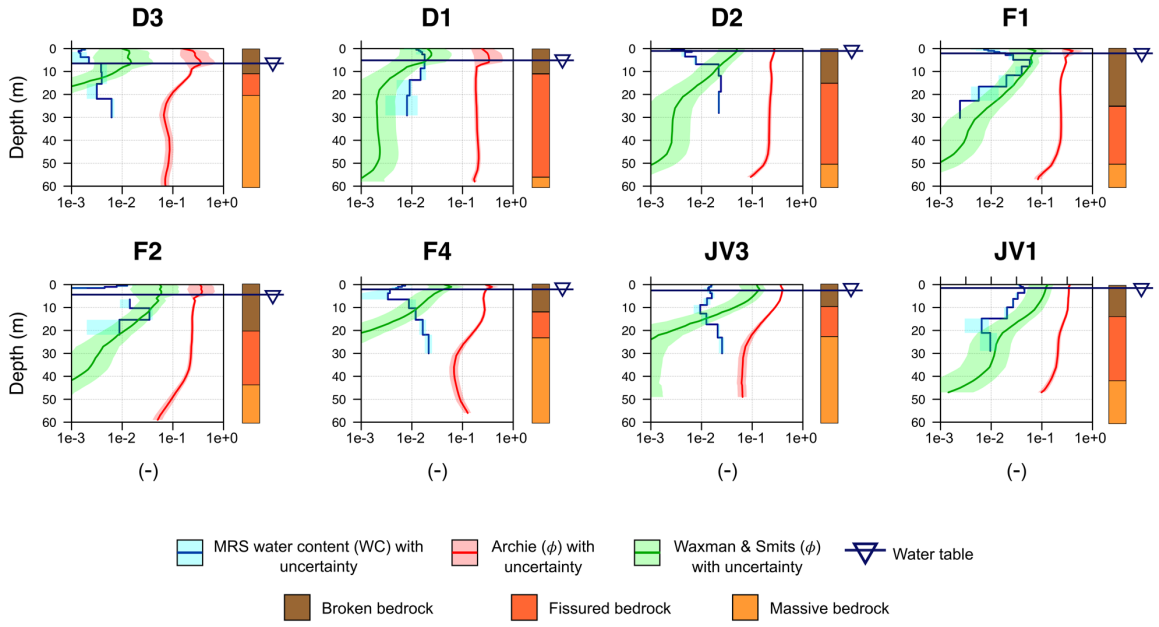


**Figure 11.** Comparison between MRS water content and ERT porosity for Archie's model and Waxman & Smits model (total porosity, including saturated and unsaturated porosity).

627 4.5. *Model comparison with storativity values from hydraulic tests*

628 Comparison of storativity data, porosity models and water content showed that Archie´s porosities
629 poorly matched observed storativity values, with values always higher by an order of magnitude in all
630 the zones of the aquifer (BB, FB, and MB) and systematically out of the variability range (Fig. 12).
631 On the other hand, Waxman & Smits porosities, displaying lower values than Archie´s model,
632 matched reasonably well the storativity values, especially in the broken and fissured bedrock. WS
633 porosities in the massive bedrock were lower by an order of magnitude but close in the upper limit of
634 the variability range. MRS water content profiles generally underestimated storativity values close to
635 the surface (BB) but had a strong correlation between storativity and porosity at larger depth (FB, $r$ =
636 0.97 and MB, $r$ = 0.98).

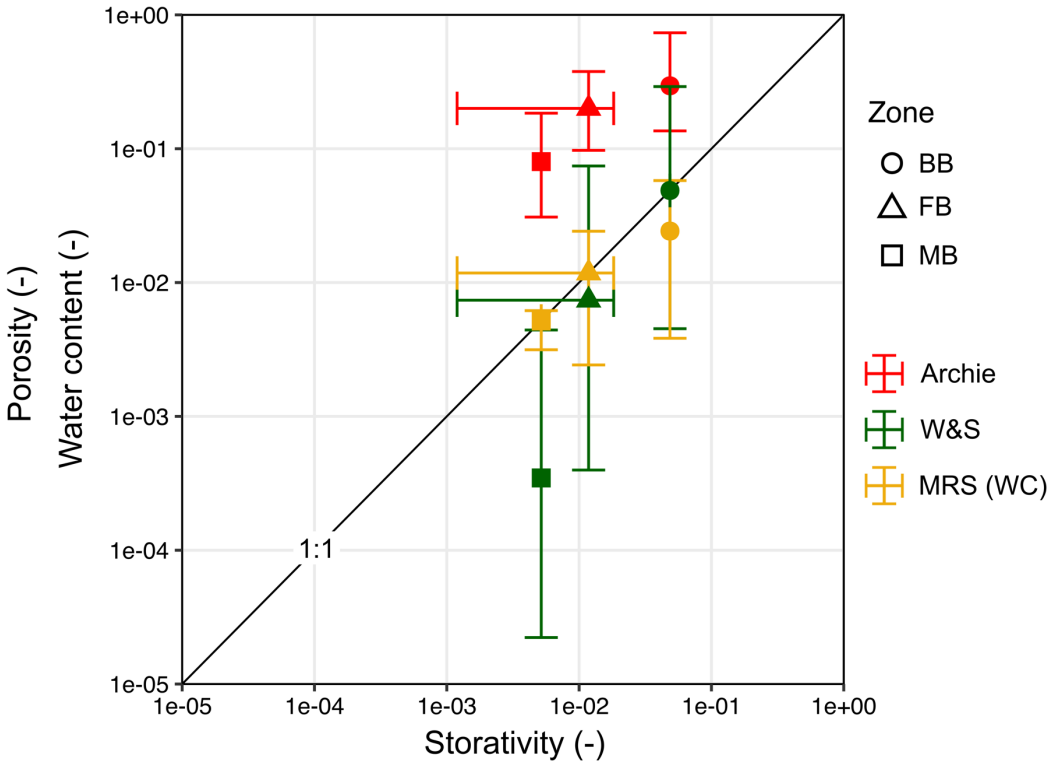


637

638 **Figure 12.** Comparison of ERT-derived porosity (Archie and Waxman & Smits porosity models) and
639 water content (MRS) per hydrogeological zone with their respective ranges of spatial variations (both
640 on vertical axis), to corresponding borehole storativity values estimated from hydraulic testing
641 (horizontal axis).

## 5. Discussion

The capability of resistivity methods to resolve pore space variability in a low porosity, basement aquifer system with spatial variations in weathering and fracturing intensity has been explored using hydrogeological and geophysical data acquired in a fractured metamorphic hard rock aquifer in Ireland. This study demonstrates that Waxman & Smits´ petrophysical model is superior to Archie´s model because of the presence of clay minerals associated with bedrock weathering, which is generalizable to most weathered/fractured basement aquifer systems.

### 5.1. *Importance of conceptual constraints when combining borehole data with 2D geophysical data*

Interpolation of point (borehole) petrophysical data was required to provide inputs for the 2D petrophysical models to obtain 2D porosity distributions from 2D ERT resistivity. Both the interpolation algorithms and the integration of structural constraints based on conceptual interpretation of geophysical data as part of the interpolation had a high impact on the spatial distribution of the parameters across the study area. Combining borehole data and a geological interpretation increased the accuracy of the distribution (Boyd et al. 2019) while showing where the geological interpretations (3-zone vs 5-zone) made the higher impact. Triangular interpolation and kriging methods produced unrealistic distributions lacking geologic sense, the nearest neighbor algorithm achieved a superior spatial distribution of the data for both Archie and Waxman & Smits models. The results exposed the fact that the absence in the interpolation of structural constraints based on hydrogeological boundaries produced spatial distributions of parameters that are geologically unrealistic as the interpolation tends to yield straight lateral continuity between boreholes, which disagreed with the structural information provided by ERT data. Constraining the models with structural boundaries is the most important tool to control the distribution of the parameters and it should be based on reliable data as is the case of this study (ERT survey). This is demonstrated when two alternative hydrogeological interpretations assuming a 3-zone and a 5-zone

668 layering are incorporated as structural constraints in the interpolation of the input parameters, which
669 produced a spatial distribution consistent with the conceptual models. As demonstrated by Chen et al.
670 (2019) using structural constraints in the interpolation helped to achieve a much more realistic
671 distribution of the parameters (*CEC, m,* $\rho_g$, $R_w$, and *T*) that follows the geological structures of the
672 study site than a non-structurally constrained interpolation. The difference between the two
673 structurally-constrained models is only observable in the area surrounding GO3 borehole, where
674 glacial deposits and alluvium are present. It is however important to note that despite being
675 geologically more realistic, structurally-constrained interpolations also likely exacerbate the contrasts
676 in petrophysical properties, and ultimately in the final computed porosities, between the different
677 conceptual bedrock units as compared to a possible smoother reality.

678

679 5.2. *Importance of accounting for clay minerals and related uncertainties*

680 Results of this study show that Archie's porosity values ($1.7 \times 10^{-1}$, i.e. 17%, in average) are
681 unrealistic because well above (1) expected porosities for weathered/fractured basement rock aquifers
682 and (2) independent geophysics data (MRS) and borehole hydraulic data obtained on the site.
683 According to Palacky (1988), hard rock aquifers are characterized by an average porosity < 4% ($4 \times$
684 $10^{-2}$). Porosity ranging between 2-4% were reported by laboratory tests carried out by Bagde (2000) in
685 three types of schists (quartz mica schist, quartz mica schist with quartz veins and biotite schist), a
686 range of porosities that matches the ERT porosities derived in this work from the Waxman & Smits
687 model. Johnson (1983) reported low porosity (3%) for metamorphic rocks, and particularly mica
688 schists with values < 1% (Elbra et al., 2011), which is again consistent with the porosity values
689 predicted by Waxman & Smits. Nevertheless, the most important distinction between the two models
690 (Archie and W&S) is that the latter accounts for the effect of clays minerals, which significantly
691 contribute to the measured resistivity similarly as pore fluid. In this study, Waxman & Smits model
692 shows that the clay in the bedrock aquifer reduces the porosity predicted from Archie's model by an
693 order of magnitude, decreasing with depth as fracture density reduces.

694 Sensitivity and uncertainty analysis were only performed for the 3-units conceptual model for both
695 Archie and Waxman & Smits. The low variability of the results and small areas that represents the
696 glacial deposits and alluvium which were accounted for in the 5-unit conceptual model do not have a
697 considerable influence in the final porosity models. The sensitivity analysis demonstrates that Archie
698 is less affected by variations in the input petrophysical parameters than Waxman & Smits. Despite
699 both being more sensitive to changes in the cementation exponent (Chen & Fang, 1986), Waxman &
700 Smits overall has higher sensitivity due to the additional factors in the equation accounting for the
701 clay content (CEC), a product of the bedrock weathering. Therefore, to build an accurate model, it is
702 necessary to well constrain the estimates for the cementation exponent for both models and the
703 influence of clay for Waxman & Smits in order to reduce uncertainty in the results. In the present
704 analysis, the large uncertainty relating to clay properties (CEC) has a large impact on the porosity
705 estimate uncertainty in the Waxman & Smits model, whereas, with the Archie model, all parameters
706 have an equivalent contribution to porosity uncertainty. At shallow depth within the unsaturated zone
707 (< 10 m), high uncertainty in the values of saturation also largely contributed to porosity uncertainty
708 for both models. However, as the unsaturated zone is relatively thin in the study area, it did not have a
709 large impact on the overall relative uncertainty.

710

711 ### 5.3. *Reconciling the different types of storage properties to which the different methods (ERT,*
712 *MRS, hydraulic tests) are sensitive*

713 The predicted 2D porosity distributions were further verified through comparison to independent
714 subsurface water content data provided by MRS surveys (Legchenko et al., 2017) (Fig. 11). The water
715 content estimates provided by MRS are considered to reflect a part of the effective saturated porosity
716 of a reservoir corresponding to mobile water (close to the storativity) (Legchenko et al., 2002;
717 Vouillamoz et al., 2012), whereas resistivity-derived porosities are widely considered as reflecting the
718 total saturated porosity of the aquifer including mobile and bound water (Turesson, 2006). This
719 implies that the ERT-porosity estimate cannot be expected to be lower than the storativity, and the
720 MRS water content estimates can be equal or lower than the ERT-derived porosities. Johnson (1983)

721 reported from laboratory experiments implemented on several samples of metamorphic rocks (mica
722 schist, muscovite schists, gneiss, etc.) an average total porosity 35% higher than the connected
723 effective porosity. The Waxman & Smits model produced overall porosity values closer to the MRS
724 water content estimates, though generally higher by about 40% on average, which is consistent with
725 the findings by Johnson (1983). The agreement between W&S and MRS porosities is particularly
726 good for soundings F1, F2, and JV1 (Fig. 11). These specific locations are characterized by areas with
727 relatively higher porosity (> 4%) and thicker BB (12-25 m) and FB (10-30 m) units associated with
728 regional fracture systems (Comte et al., 2012a, 2019). At larger depths (MB) for these locations, the
729 uncertainty of MRS water content (but also of ERT-derived porosity) increased and the correlation
730 between the two is poor, with ERT porosity significantly higher than MRS water content. This
731 deviation could be attributed to the decrease in fracture connectivity with depth in the massive
732 bedrock resulting in a more rapid decrease in effective porosity and/or storativity versus total porosity
733 and associated loss of sensitivity of the MRS method (Legchenko et al., 2002). In the other 5 profiles
734 (D1, D2, D3, F4, and JV3), there are some incongruities between the ERT-porosities and MRS water
735 content. These locations were further away from deeper weathered/fractured zones and characterized
736 by overall lower water content close to or lower than 1%. There, MRS water content appeared
737 relatively constant or increasing with depth and was much higher than ERT-derived porosities.
738 However, the MRS method is known to rapidly lose sensitivity below 1% water content where data
739 inversion becomes unreliable (Legchenko et al., 2006). Similarly, ERT-derived porosities could be
740 underestimated in these areas particularly for the massive bedrock due to the ERT inversion tending to
741 overestimate resistivities below conductive material (FB). Both could explain the large deviation at
742 depth at these locations.

743 The overall comparison is consistent with current knowledge that resistivity-derived porosity provides
744 a close estimate of total porosity (Ellis and Singer, 2007; He et al., 2018) and as such should be higher
745 than or equal to the aquifer's effective groundwater storage (storativity). For most of our presented
746 results, the ERT-derived porosities are indeed equal to or higher than the MRS water content known
747 to be reflective of aquifer storativity rather than total saturated porosity. More specifically the

748 porosities obtained from the application of the Waxman & Smits model are consistent with the
749 expected difference between effective and total porosity in fractured rocks of about a factor of 2
750 (Aguilera and Aguilera, 2003; Tiab et al., 2006); whereas Archie's model is shown to massively
751 overestimate this difference by a factor of 10 (an order of magnitude) demonstrating that clay
752 minerals cannot be neglected in the analysis of similar metamorphic rock aquifer settings.

753 Further comparison of the results with actual aquifer storativity values previously obtained from
754 hydraulic testing at borehole locations by Comte et al. (2012a) confirmed Archie´s model poor
755 predicting ability of storage properties. Waxman & Smits porosities in contrast show a good match
756 with storativities obtained in the broken and fissured bedrock (the weathered-fractured part of the
757 system). This would suggest either that the porosity derived from this model in this upper part of the
758 bedrock is reflective of the aquifer's effective storage capacity rather than the total porosity (including
759 bound and unconnected groundwater), or that storativity and total porosity are not significantly
760 different in these horizons. However, it is also likely that storativity values obtained from hydraulic
761 testing are providing an overestimation of the actual aquifer storativity due to being representative of
762 a small area abound the boreholes (because of the low pumping rates applicable for hydraulic testing
763 such low productivity hydrogeological environment) affected by locally increased porosity associated
764 to the downhole hammer drilling technique (Kirlas and Katsifarakis, 2020; Pongmanda and Suprapti,
765 2020). Such artificially increased porosity and storativity would have relatively more effect on deeper
766 (more massive) than shallower bedrock horizons. In the MB specifically, WS-derived porosities
767 appeared much lower than storativity values. This difference could indeed be due to; (1) as also
768 discussed above when comparing ERT porosity and MRS water content, an underestimation of
769 porosity in the MB due to overestimation of inverted resistivities below the lower resistivity FB
770 together with the uncertainty attributed to the selection of *m* for the MB; or (2) overestimated
771 storativities values from hydraulic testing in the MB (artificially increased porosity in the borehole
772 walls, and local preferential pathways possible due to the large uncased interval characterizing MB
773 boreholes). MRS water content on another hand is relatively close to storativity values in the FB and
774 MB. Based on discussions above, the good match for MB might be coincidental due to both (1) a

775 possible overestimation of MRS water content in the MB, where MRS profiles often showed illogical
776 increasing water content with depth likely resulting from lack of accuracy of the MRS inversions
777 (Legchenko et al., 2017) for low water content values; (2) a possible overestimation of storativity
778 from hydraulic tests in the MB. MRS water content also appeared slightly lower than storativities in
779 the BB. Overall, it can be reasonably concluded that the WS porosity provides an upper estimate of
780 groundwater storage in the weathered/fractured aquifer units (BB and FB).

781

782 5.4. *Limitations associated to field measurements and geophysical inversion errors and wider*
783 *application to 3D heterogeneous hard rock aquifer settings*

784 Modelling petrophysical properties is a challenging process. The high heterogeneity of
785 weathered/fractured aquifers complicates any attempt to estimate properties, as in this study porosity
786 (Paillet and Reese, 2000; Doetsch et al., 2010; Whitman and Yeboah-Forson, 2015). This study
787 encountered limitations typical to field studies in heterogeneous subsurface systems, attributed to: (1)
788 uncertainties in point-based measurements of parameters used to parameterize the porosity models
789 (cementation exponent and clay volumes); (2) uncertainty and representativity issues relating to
790 storativities values obtained from low rate hydraulic testing used for verification, which are likely
791 overestimations increasing with depth (i.e. with decreasing porosity) (3) poor spatial density of
792 borehole data providing the petrophysical input parameters and storativity verification data; (4) spatial
793 distortions and errors relating to inverted geophysical data used as model input parameters (different
794 averaging between ERT and MRS; ERT use 2-D inversion and MRS 1-D inversion, both in 3-D
795 geological settings); and (5) possible additional uncertainty attributed to the geophysical measures
796 errors (noise) prior to geophysical inversion (negligible in this work but potentially significant in
797 other, more noisy conditions, e.g. drier/more resistant soils and anthropogenic noise). Addressing
798 some of these limitations would reduce uncertainty, providing more accurate values in porosity
799 models. Acquiring more data does not always translate into better results, but in this study having
800 additional borehole data in a reduced spacing would help to control the spatial distribution and
801 increase the resolution of the models, along with providing additional verification dataset.

802 The one- and two- dimensionalities of data and models used might be insufficient in some strongly
803 three-dimensional settings, which would require 3D ERT acquisition. In this case study, however,
804 previous hydrogeological studies (Comte et al., 2012a, 2019) suggest lateral continuity of structures
805 perpendicular to the ERT profile justifying the use of 2D ERT data. Similarly, more confident
806 validation with borehole and MRS data would be obtained from denser 2D borehole coverage and 2D
807 MRS acquisition and inversion, with 3D borehole and 3D MRS analyses required for other strongly
808 3D basement settings. The approach developed overall is applicable to most basement aquifer settings
809 and bedrock lithologies subject to a certain degree of weathering. Some challenges would arise in; (1)
810 deeply weathered, argillized basement rocks such as clay rich metamorphic rocks subject to deep
811 tropical weathering, where ERT inversion would be inaccurate below highly conductive weathering
812 clays (Bazin and Pfaffhuber, 2013) resulting in poor delineation of weathered vs. fractured vs.
813 massive bedrock and inaccurate quantification of storage properties (2) unweathered, poorly fractured
814 basement rocks such as crystalline rocks subject to glacial erosion preventing development of
815 significant weathering and weathering-aided open fracture networks. Nevertheless, the flexibility of
816 the ERT methods allowing adjusting its resolution to the expected scale of heterogeneity (Chambers
817 et al., 2010; Cheng et al., 2019) makes it a useful technique for a range of heterogeneous basement
818 settings from local-scale variations of fracture density and weathering to regional fault zones.

819 The higher uncertainty in the approach is attributed to the clay content of the aquifer with limited data
820 from boreholes to directly estimate mineralogy and clay volume spatial variability in the subsurface
821 with high accuracy. Implementing an alternative geophysical method (e.g., induced polarization)
822 providing additional constraints on clay content and/or electrical properties could improve the
823 outcome of the Waxman & Smits model (Binley et al., 2015; Revil et al., 2019).

824

825 ### 5.5. *Transferability of methods and findings*

826 Although the methodology developed in this study was applied to a specific location, the approach
827 can be extended to most basement rock aquifer settings. All basement rocks (intrusive igneous and

828 metamorphic rocks such as gneiss, granite, schist) are affected by carriable degree of weathering and
829 fracturing responsible to a weathering profile as described in Fig. 2, and more generically by e.g.
830 Lachassagne et al. (2011), which is globally ubiquitous. A possible exception are basement rocks
831 freshly exposed after deep glacial erosion, which may have been completely removed of their
832 weathering profile at the exception of the bottommost fresh massive bedrock. Electrical (e.g. ERT)
833 and electromagnetic geophysical methods are well-established techniques effective to delineate these
834 weathering patterns in various basement rock types and climate setting (Beauvais et al., 2004; Undul
835 et al., 2011; Belle et al., 2019). Consequently, the present approach may be potentially implemented
836 in most basement settings. In addition, the approach can also be applied to any other resistivity
837 map/models obtained from other electromagnetic survey methods e.g. frequency and time domain
838 electromagnetics FEM/TEM, magneto-telluric MT (Descloitres et al., 2000; El-Kaliouby, 2009). This
839 includes data from airborne TEM whose popularity is rapidly increasing for large-scale
840 hydrogeological mapping including in basement rocks (Chandra et al., 2019). A limitation of the
841 approach however is the need for data on bedrock clay content and mineralogy, and importantly their
842 spatial variations, necessary for CEC estimation required for the Waxman & Smits model. While
843 some data may be obtained from literature for the considered site or extrapolated from other regions,
844 additional in situ investigations are recommended. This include analysis of core sample and borehole
845 geophysics to estimate vertical clay properties variation along the weathering profile. Alternative
846 geophysical methods (e.g. induced polarization) may profile information on clay content and CEC
847 (Revil et al., 2019). The present work also shows that the MRS method (distributed vertical sounding
848 or tomography) could also be used to calibrate either the Waxman and Smits model, or directly the
849 porosity/water content, within or across lithotypes, for subsequent large-scale porosity modelling
850 using high resolutions resistivity data.

851

852 **6. Conclusions**

853 This study explored the qualitative and quantitative the use of electrical resistivity tomography to
854 assess groundwater storage variations at high spatial resolution in a weathered/fractured basement

855 rock aquifer in Ireland, using the two most commonly applied petrophysical models to relate
856 resistivity to porosity: Waxman and Smits (1968), which accounts for the influence of clay minerals
857 produced by weathering processes, and Archie (1942), which disregards clays.

858 Results show that ERT was capable of qualitatively delineating at high (2D vertical) spatial resolution
859 the variability in porosity associated to depth-decreasing weathering and fracturing and as well as
860 local deeper weathered/fracture zones. On a quantitative level, the use of the WS model with ERT
861 data provided a reasonable upper-bound estimate of storage properties values (storativities) in the
862 weathered/fractured parts of the bedrock (~5 to 50+ m in the studied area). These values were shown
863 to range across 2 to 3 orders of magnitude from typically 1-10% in the uppermost weathered 'broken
864 bedrock' to 0.1-1% in the underlying fissured bedrock, and further down by another order of
865 magnitude lower in the deep massive bedrock. These values were broadly consistent with independent
866 storativities estimates for the weathered/fractured aquifer levels provided by magnetic resonance
867 soundings (at 8 locations) and borehole hydraulic testing (9 data including 3 different depths at 3
868 sites). These values are consistent with reported typical values for hard rock settings. This work
869 further resolves the large spatial (including depth) variability in storage properties that may be
870 encountered in basement aquifer settings, at high spatial resolution and with reasonable uncertainties,
871 i.e. an overall exponential decrease in storativity with depth and with distance to valley bottom to
872 which superimposes smaller, meter to 100-meter scale, variability related to deep weathering
873 corridors associated with fault lines. Some inconsistencies however were found in the storativities
874 values provided by all three methods in the deep massive bedrock owing to limitations and
875 inaccuracies specific to each method, which prevented any reliable quantification in this deepest unit.

876 More specifically, the study highlighted the inadequacy of Archie's model to derive porosity from
877 resistivity in weathered/fractured aquifers, for which Waxman and Smits model, which accounts for
878 the major effect of clay mineral on resistivity data, must be preferred.

879 The choice of the method of interpolation of point (borehole) input parameters for the petrophysical
880 models, along with the use of structural constraints in the interpolation based on hydrogeological
881 conceptual interpretation of ERT data, also proved crucial to obtaining realistic porosity distributions.

Both petrophysical models were found to be highly sensitive to the cementation factor, however, because of its reported low variability for basement settings this did not have the highest impact on porosity prediction uncertainties. Instead, the clay content and CEC (for WS model) were responsible for the largest source of uncertainty in predicting porosity from resistivity highlighting the need for in situ data on bedrock mineralogy (including clay content and minerals). Relative uncertainty increased in two directions, vertically with depth, and laterally from downhill to uphill, and this concurrently to porosity decrease due to increasing relative importance of uncertainties of cementation factor and in clay properties.

This study also provides an example of how the combination of near surface geophysical methods (here ERT and MRS), can contribute to achieving a better interpretation of the storage properties values and spatial variability of low storage weathered/fractured hard rock aquifers. The approach can be extended to resistivity imaging methods in a wide sense, i.e. not only ERT but by extension also electromagnetic methods (e.g. frequency/time domain EM) that yield resistivity models, which can be used with WS to derive porosity models.

Characterizing hard rock aquifers remains challenging, and the limited number of published *in situ* quantitative research suggests that more work needs to be done to understand these groundwater resources and specifically the *in situ* spatial variability of hydrogeological properties. Estimating spatial porosity patterns is a crucial step in quantifying the distribution and volume of groundwater resources in hard rock aquifers required to support sustainable potable water supplies, agriculture/livestock farming, environmental flows and groundwater dependent ecosystems, geothermal applications, etc., but also to predict the response of these resources to short and long term changes in climate, including climate variability and human exploitation.

## 7. Acknowledgments

We thank the National Council of Science and Technology and Secretariat of Energy of México (CONACYT-SENER) for funding this research, and the Geological Survey of Ireland and MSc

908 students at Queen's University of Belfast for assistance in data collection. We appreciate the
909 insightful and constructive comment by P. Lachassagne and two anonymous reviewers which
910 contributed to improve the manuscript.

911

912 **8. References**

913 Abdulaziz, A.M., Hurtado, J.M., Faid, A., 2012. Hydrogeological characterization of Gold Valley: an
914 investigation of precipitation recharge in an intermountain basin in the Death Valley region,
915 California, USA. Hydrogeol. J. 20, 701–718. https://doi.org/10.1007/s10040-012-0840-8

916 Aguilera, M.S., Aguilera, R., 2003. Improved models for petrophysical analysis of dual porosity
917 reservoirs. Petrophysics 44, 15.

918 Aguilera, R., 2008. Effect of fracture dip and fracture tortuosity on petrophysical evaluation of
919 naturally fractured reservoirs. Pet. Soc. Can. 8.

920 Aguilera, R., 1976. Analysis of naturally fractured reservoirs from conventional well logs. J. Pet.
921 Technol. 11.

922 Ahmed, S., Jayakumar, R., Salih, A., 2008. Groundwater dynamics in hard rock aquifers: sustainable
923 management and optimal monitoring network design. Springer, Dordrecht, The Netherlands.

924 Archie, G.E., 1942. The electrical resistivity log as an aid in determining some reservoir
925 Characteristics. Trans. AIME 146, 54–62. https://doi.org/10.2118/942054-G

926 Arps, J.J., 1953. The effect of temperature on the density and electrical resistivity of sodium chloride
927 solutions. J. Pet. Technol. 5, 17–20. https://doi.org/10.2118/953327-G

928 Bagde, M.N., 2000. An investigation into strength and porous properties of metamorphic rocks in the
929 Himalayas: A case study. Geotech. Geol. Eng. 18, 209–219.
930 https://doi.org/10.1023/A:1026518616345

931 Balaman, Ş.Y., 2019. Uncertainty issues in biomass-based production chains, in: Decision-making for
932 biomass-based production chains. Elsevier, pp. 113–142. https://doi.org/10.1016/B978-0-12-814278-
933 3.00005-4

934 Bazin, S., Pfaffhuber, A.A., 2013. Mapping of quick clay by electrical resistivity tomography under
935 structural constraint. J. Appl. Geophys. 98, 280–287. https://doi.org/10.1016/j.jappgeo.2013.09.002

936 Beauvais, A., Ritz, M., Parisot, J.-C., Bantsimba, C., Dukhan, M., 2004. Combined ERT and GPR
937 methods for investigating two-stepped lateritic weathering systems. Geoderma 119, 121–132.
938 https://doi.org/10.1016/j.geoderma.2003.06.001

939 Belle, P., Lachassagne, P., Mathieu, F., Barbet, C., Brisset, N., Gourry, J.-C., 2019. Characterization
940 and location of the laminated layer within hard rock weathering profiles from electrical resistivity
941 tomography: implications for water well siting. Geol. Soc. Lond. Spec. Publ. 479, 187.
942 https://doi.org/10.1144/SP479.7

943 Bibi, I., Icenhower, J., Niazi, N.K., Naz, T., Shahid, M., Bashir, S., 2016. Clay Minerals, in:
944 Environmental Materials and Waste. Elsevier, pp. 543–567. https://doi.org/10.1016/B978-0-12-
945 803837-6.00021-4

946 Binley, A., Hubbard, S.S., Huisman, J.A., Revil, A., Robinson, D.A., Singha, K., Slater, L.D., 2015.
947 The emergence of Hydrogeophysics for improved understanding of subsurface processes over
948 multiple scales. Water Resour. Res. 51, 3837–3866. https://doi.org/10.1002/2015WR017016

949 Boyd, D.L., Walton, G., Trainor-Guitton, W., 2019. Quantifying spatial uncertainty in rock through
950 geostatistical integration of borehole data and a geologist's cross-section. Eng. Geol. 260, 105246.
951 https://doi.org/10.1016/j.enggeo.2019.105246

952 Butler, J.J., 2005. Hydrogeological methods for estimation of spatial variations in hydraulic
953 conductivity, in: Rubin, Y., Hubbard, S.S. (Eds.), Hydrogeophysics. Springer, Dordrecht, The
954 Netherlands, pp. 23–58. https://doi.org/10.1007/1-4020-3102-5_2

955 Caulfield, J., Chelliah, M., Comte, J.-C., Cassidy, R., Flynn, R., 2014. Integrating petrography,
956 mineralogy and hydrochemistry to constrain the influence and distribution of groundwater
957 contributions to baseflow in poorly productive aquifers: Insights from Gortinlieve catchment, Co.
958 Donegal, NW Ireland. Sci. Total Environ. 500–501, 224–234.
959 https://doi.org/10.1016/j.scitotenv.2014.08.105

960 Chambers, J.E., Wilkinson, P.B., Wealthall, G.P., Loke, M.H., Dearden, R., Wilson, R., Allen, D.,
961 Ogilvy, R.D., 2010. Hydrogeophysical imaging of deposit heterogeneity and groundwater chemistry
962 changes during DNAPL source zone bioremediation. J. Contam. Hydrol. 118, 43–61.
963 https://doi.org/10.1016/j.jconhyd.2010.07.001

964 Chandra, S., Auken, E., Maurya, P.K., Ahmed, S., Verma, S.K., 2019. Large scale mapping of
965 fractures and groundwater pathways in crystalline hardrock by AEM. Sci. Rep. 9, 398.
966 https://doi.org/10.1038/s41598-018-36153-1

967 Chaudhuri, A., Sekhar, M., Descloitres, M., Godderis, Y., Ruiz, L., Braun, J.J., 2013. Constraining
968 complex aquifer geometry with geophysics (2-D ERT and MRS measurements) for stochastic
969 modelling of groundwater flow. J. Appl. Geophys. 98, 288–297.
970 https://doi.org/10.1016/j.jappgeo.2013.09.005

971 Chen, H.C., Fang, J.H., 1986. Sensitivity analysis of the parameters in Archie's water saturation
972 equation. Log Anal. 27, 6.

973 Chen, Y., Chen, X., Wang, Y., Zu, S., 2019. The interpolation of sparse geophysical data. Surv.
974 Geophys. 40, 73–105. https://doi.org/10.1007/s10712-018-9501-3

975 Cheng, Q., Tao, M., Chen, X., Binley, A., 2019. Evaluation of electrical resistivity tomography (ERT)
976 for mapping the soil–rock interface in karstic environments. Environ. Earth Sci. 78, 439.
977 https://doi.org/10.1007/s12665-019-8440-8

978 Christidis, G.E., 2010. Industrial Clays, in: Ferraris, G., Christidis, G.E. (Eds.), Advances in the
979 Characterization of Industrial Minerals. European Mineralogical Union, pp. 341–414.
980 https://doi.org/10.1180/EMU-notes.9.9

981 Comte, J.-C., Cassidy, R., Nitsche, J., Ofterdinger, U., Pilatova, K., Flynn, R., 2012a. The typology of
982 Irish hard-rock aquifers based on an integrated hydrogeological and geophysical approach.
983 Hydrogeol. J. https://doi.org/10.1007/s10040-012-0884-9

984 Comte, J.-C., Cassidy, R., Ofterdinger, U., Wilson, C., Nitsche, J., 2012b. A combined Dipole-
985 Dipole/multi-Gradient ERT array optimised for the hydrogeological characterisation of hard rock
986 aquifers. Presented at the International Conference of Groundwater in Fractured Rocks, Prague, Cezch
987 Republic. https://doi.org/10.13140/2.1.1420.4169

988 Comte, J.-C., Ofterdinger, U., Legchenko, A., Caulfield, J., Cassidy, R., Mézquita González, J.A.,
989 2019. Catchment-scale heterogeneity of flow and storage properties in a weathered/fractured hard
990 rock aquifer from resistivity and magnetic resonance surveys: implications for groundwater flow
991 paths and the distribution of residence times. Geol. Soc. Lond. Spec. Publ. 479, 35–58.
992 https://doi.org/10.1144/SP479.11

993 Day-Lewis, F.D., Slater, L.D., Robinson, J., Johnson, C.D., Terry, N., Werkema, D., 2017. An
994 overview of geophysical technologies appropriate for characterization and monitoring at fractured-
995 rock sites. J. Environ. Manage. 204, 709–720. https://doi.org/10.1016/j.jenvman.2017.04.033

996 Descloitres, M., Guérin, R., Albouy, Y., Tabbagh, A., Ritz, M., 2000. Improvement in TDEM
997 sounding interpretation in presence of induced polarization. A case study in resistive rocks of the
998 Fogo volcano, Cape Verde Islands. J. Appl. Geophys. 45, 1–18. https://doi.org/10.1016/S0926-
999 9851(00)00015-X

1000 Descloitres, M., Ruiz, L., Sekhar, M., Legchenko, A., Braun, J.-J., Mohan Kumar, M.S.,
1001 Subramanian, S., 2008. Characterization of seasonal local recharge using electrical resistivity
1002 tomography and magnetic resonance sounding. Hydrol. Process. 22, 384–394.
1003 https://doi.org/10.1002/hyp.6608

1004 Dewandel, B., Lachassagne, P., Zaidi, F.K., Chandra, S., 2011. A conceptual hydrodynamic model of
1005 a geological discontinuity in hard rock aquifers: Example of a quartz reef in granitic terrain in South
1006 India. J. Hydrol. 405, 474–487. https://doi.org/10.1016/j.jhydrol.2011.05.050

1007 Doetsch, J., Linde, N., Coscia, I., Greenhalgh, S.A., Green, A.G., 2010. Zonation for 3D aquifer
1008 characterization based on joint inversions of multimethod crosshole geophysical data. Geophysics 75,
1009 G53–G64. https://doi.org/10.1190/1.3496476

1010 Dolcater, D.L., Jackson, M.L., Syers, J.K., 1972. Cation exchange selectivity in mica and vermiculite.
1011 Am. Mineral. 57, 1823–1831.

1012 Earle, S., 2015. Physical geology. BCcampus, Victoria, B.C.

1013 Elbra, T., Karlqvist, R., Lassila, I., Hæggström, E., Pesonen, L.J., 2011. Laboratory measurements of
1014 the seismic velocities and other petrophysical properties of the Outokumpu deep drill core samples,
1015 eastern Finland. Geophys. J. Int. 184, 405–415. https://doi.org/10.1111/j.1365-246X.2010.04845.x

1016 El-Kaliouby, H., 2019. Groundwater prospecting in a hard-rock coastal area using off-set TDEM
1017 method: Case study, in: SEG Technical Program Expanded Abstracts 2019. Presented at the SEG
1018 Technical Program Expanded Abstracts 2019, Society of Exploration Geophysicists, San Antonio,
1019 Texas, pp. 2755–2758. https://doi.org/10.1190/segam2019-3209246.1

1020 Ellis, D.V., Singer, J.M., 2007. Well logging for earth scientists, 2nd ed. Springer, Dordrecht, The
1021 Netherlands.

1022 Flinchum, B.A., Holbrook, W.S., Grana, D., Parsekian, A.D., Carr, B.J., Hayes, J.L., Jiao, J., 2018.
1023 Estimating the water holding capacity of the critical zone using near-surface geophysics. Hydrol.
1024 Process. 32, 3308–3326. https://doi.org/10.1002/hyp.13260

1025 Flinchum, B.A., Holbrook, W.S., Parsekian, A.D., Carr, B.J., 2019. Characterizing the critical zone
1026 using borehole and surface nuclear magnetic resonance. Vadose Zone J. 18, 1–18.
1027 https://doi.org/10.2136/vzj2018.12.0209

Geffray, C., Gerschenfeld, A., Kudinov, P., Mickus, I., Jeltsov, M., Kööp, K., Grishchenko, D., Pointer, D., 2019. Verification and validation and uncertainty quantification, in: Thermal Hydraulics Aspects of Liquid Metal Cooled Nuclear Reactors. Elsevier, pp. 383–405. https://doi.org/10.1016/B978-0-08-101980-1.00008-9

Gleick, P.H., 1993. Water in Crisis: A Guide to the World's Fresh Water Resources, illustrated. ed. Oxford University Press.

Glover, P., 2009. What is the cementation exponent? A new interpretation. Lead. Edge 28, 82–85. https://doi.org/10.1190/1.3064150

He, R., Ma, H., Hafiz, R.B., Fu, C., Jin, X., He, J., 2018. Determining porosity and pore network connectivity of cement-based materials by a modified non-contact electrical resistivity measurement: Experiment and theory. Mater. Des. 156, 82–92. https://doi.org/10.1016/j.matdes.2018.06.045

Johnson, G.R., 1983. Rock property measurements and analysis of selected igneous, sedimentary, and metamorphic rocks from worldwide localities (Report No. 83–736), Open-File Report. https://doi.org/10.3133/ofr83736

Jørgensen, S.E., Fath, B.D., 2011. Concepts of Modelling, in: Developments in Environmental Modelling. Elsevier, pp. 19–93. https://doi.org/10.1016/B978-0-444-53567-2.00002-8

Kazakis, N., Vargemezis, G., Voudouris, K.S., 2016. Estimation of hydraulic parameters in a complex porous aquifer system using geoelectrical methods. Sci. Total Environ. 550, 742–750. https://doi.org/10.1016/j.scitotenv.2016.01.133

Kirlas, M.C., Katsifarakis, K.L., 2020. Evaluation of automated groundwater level measurements for transmissivity and storativity calculation. J. Water Supply Res. Technol.-Aqua. https://doi.org/10.2166/aqua.2020.100

Kirsch, R., 2009. Groundwater geophysics: a tool for hydrogeology, 2nd ed. Springer, Berlin, Heidelberg.

1052 Krásný, J., Sharp, J.M., 2007. Hydrogeology of fractured rocks from particular fractures to regional
1053 approaches: State-of-the-art and future challenges, in: Groundwater in Fractured Rocks. CRC Press,
1054 pp. 1–30.

1055 Krásný, J., Sharp, J.M., Troeger, U., 2014. IAH Commission on Hardrock Hydrogeology (HyRoC):
1056 Past and present activities, future possibilities, in: Fractured Rock Hydrogeology, Selected Papaers in
1057 Hydrogeology. CRC Press, The Netherlands, pp. 1–12.

1058 Kumar, D., Mondal, S., Nandan, M.J., Harini, P., Sekhar, B.M.V.S., Sen, M.K., 2016. Two-
1059 dimensional electrical resistivity tomography (ERT) and time-domain-induced polarization (TDIP)
1060 study in hard rock for groundwater investigation: a case study at Choutuppal Telangana, India. Arab.
1061 J. Geosci. 9, 355. https://doi.org/10.1007/s12517-016-2382-1

1062 Lachassagne, P., 2008. Overview of the hydrogeology of hard rock aquifers: applications for their
1063 survey, management, modelling and protection, in: Ahmed, S., Jayakumar, R., Salih, A. (Eds.),
1064 Groundwater dynamics in hard rock aquifers: sustainable management and optimal monitoring
1065 Network Design. Springer, Dordrecht, The Netherlands, pp. 40–63. https://doi.org/10.1007/978-1-
1066 4020-6540-8_3

1067 Lachassagne, P., Dewandel, B., Wyns, R., 2014. The conceptual model of weathered hard rock
1068 aquifers and its practical applications, in: Sharp, J.M. (Ed.), Fractured Rock Hydrogeology, Selected
1069 Papers in Hydrogeology. CRC Press, Taylor and Francis Group, The Netherlands, pp. 13–46.
1070 https://doi.org/10.1201/b17016-3

1071 Lachassagne, P., Wyns, R., Bérard, P., Bruel, T., Chéry, L., Coutand, T., Desprats, J.-F., Le Strat, P.,
1072 2001. Exploitation of high-yields in hard-rock aquifers: downscaling methodology combining GIS
1073 and multicriteria analysis to delineate field prospecting zones. Groundwater 39, 568–581.
1074 https://doi.org/10.1111/j.1745-6584.2001.tb02345.x

1075 Lachassagne, P., Wyns, R., Dewandel, B., 2011. The fracture permeability of Hard Rock Aquifers is
1076 due neither to tectonics, nor to unloading, but to weathering processes: Weathering and permeability
1077 of Hard Rock Aquifers. Terra Nova 23, 145–161. https://doi.org/10.1111/j.1365-3121.2011.00998.x

1078 Legchenko, A., Baltassat, J.-M., Beauce, A., Bernard, J., 2002. Nuclear magnetic resonance as a
1079 geophysical tool for hydrogeologists. J. Appl. Geophys. 50, 21–46. https://doi.org/10.1016/S0926-
1080 9851(02)00128-3

1081 Legchenko, A., Comte, J.-C., Ofterdinger, U., Vouillamoz, J.-M., Lawson, F.M.A., Walsh, J., 2017.
1082 Joint use of singular value decomposition and Monte-Carlo simulation for estimating uncertainty in
1083 surface NMR inversion. J. Appl. Geophys. 144, 28–36. https://doi.org/10.1016/j.jappgeo.2017.06.010

1084 Legchenko, A., Descloitres, M., Bost, A., Ruiz, L., Reddy, M., Girard, J.-F., Sekhar, M., Mohan
1085 Kumar, M.S., Braun, J.-J., 2006. Resolution of MRS applied to the characterization of hard-rock
1086 aquifers. Groundwater 44, 547–554. https://doi.org/10.1111/j.1745-6584.2006.00198.x

1087 Legchenko, A., Descloitres, M., Vincent, C., Guyard, H., Garambois, S., Chalikakis, K., Ezersky, M.,
1088 2011. Three-dimensional magnetic resonance imaging for groundwater. New J. Phys. 13, 025022.
1089 https://doi.org/10.1088/1367-2630/13/2/025022

1090 Leopold, M., Völkel, J., Huber, J., Dethier, D., 2013. Subsurface architecture of the Boulder Creek
1091 Critical Zone Observatory from electrical resistivity tomography. Earth Surf. Process. Landf. 38,
1092 1417–1431. https://doi.org/10.1002/esp.3420

1093 MacDonald, A.M., Davies, J., 2000. A brief review of groundwater for rural water supply in sub-
1094 Saharan Africa (Technical Report No. WC/00/33). BGS.

1095 Massuel, S., Favreau, G., Descloitres, M., Le Troquer, Y., Albouy, Y., Cappelaere, B., 2006. Deep
1096 infiltration through a sandy alluvial fan in semiarid Niger inferred from electrical conductivity survey,
1097 vadose zone chemistry and hydrological modelling. CATENA 67, 105–118.
1098 https://doi.org/10.1016/j.catena.2006.02.009

1099 Meunier, A., 2005. Clays. Springer, Berlin, Heidelberg.

1100 Moe, H., Craig, M., Daly, D., 2010. Poorly productive aquifers summary report. CDM and the
1101 Environmental Protection Agency, Dublin.

1102 Moreno-Maroto, J.M., Alonso-Azcárate, J., 2018. What is clay? A new definition of “clay” based on
1103 plasticity and its impact on the most widespread soil classification systems. Appl. Clay Sci. 161, 57–
1104 63. https://doi.org/10.1016/j.clay.2018.04.011

1105 Ofterdinger, U., Macdonald, A., Comte, J.-C., Young, M., 2019. Groundwater in fractured bedrock
1106 environments: managing catchment and subsurface resources. Geol. Soc. Lond. Spec. Publ. 479,
1107 SP479-2018. https://doi.org/10.1144/SP479-2018-170

1108 Oldenburg, D.W., Li, Y., 1999. Estimating depth of investigation in dc resistivity and IP surveys.
1109 Geophysics 64, 403–416. https://doi.org/10.1190/1.1444545

1110 Paillet, F.L., Reese, R.S., 2000. Integrating borehole logs and aquifer tests in aquifer characterization.
1111 Groundwater 38, 713–725. https://doi.org/10.1111/j.1745-6584.2000.tb02707.x

1112 Palacky, G.J., 1988. Resistivity characteristics of geologic targets, in: Electromagnetic Methods in
1113 Applied Geophysics: Volume 1, Theory, Investigations in Geophysics. Society of Exploration
1114 Geophysicists, pp. 52–129. https://doi.org/10.1190/1.9781560802631.ch3

1115 Pellerin, L., 2002. Applications of electrical and electromagnetic methods for environmental and
1116 geotechnical investigations. Surv. Geophys. 32.

1117 Piedrahita, J., Aguilera, R., 2017. A petrophysical dual-porosity model for evaluation of secondary
1118 mineralization and tortuosity in naturally fractured reservoirs. SPE-180242-PA 20, 304–316.
1119 https://doi.org/10.2118/180242-PA

1120 Pisani, L., 2011. Simple expression for the tortuosity of porous media. Transp. Porous Media 88, 193–
1121 203. https://doi.org/10.1007/s11242-011-9734-9

1122 Pongmanda, S., Suprapti, A., 2020. Performing application of cooper-jacob method for identification
1123 of storativity. IOP Conf. Ser. Earth Environ. Sci. 419, 012128. https://doi.org/10.1088/1755-
1124 1315/419/1/012128

Revil, A., Cathles III, L.M., Losh, S., Nunn, J.A., 1998. Electrical conductivity in shaly sands with geophysical applications. J. Geophys. Res. Solid Earth 103, 23925–23936. https://doi.org/10.1029/98JB02125

Revil, A., Qi, Y., Ghorbani, A., Coperey, A., Ahmed, A.S., Finizola, A., Ricci, T., 2019. Induced polarization of volcanic rocks. 3. Imaging clay cap properties in geothermal fields. Geophys. J. Int. 218, 1398–1427. https://doi.org/10.1093/gji/ggz207

Robert, T., Caterina, D., Deceuster, J., Kaufmann, O., Nguyen, F., 2012. A salt tracer test monitored with surface ERT to detect preferential flow and transport paths in fractured/karstified limestones. Geophysics 77, B55–B67. https://doi.org/10.1190/geo2011-0313.1

Rubin, Y., Hubbard, S.S., 2005. Hydrogeophysics, Water science and technology library. Springer, Dordrecht, The Netherlands.

Salem, H.S., 2001. Determination of porosity, formation resistivity factor, archie cementation factor, and pore geometry factor for a glacial aquifer. Energy Sources 23, 589–596. https://doi.org/10.1080/00908310152125238

Salem, H.S., Chilingarian, G.V., 1999. The cementation factor of Archie's equation for shaly sandstone reservoirs. J. Pet. Sci. Eng. 23, 83–93. https://doi.org/10.1016/S0920-4105(99)00009-1

Schön, J.H., 2015. Density, in: Developments in Petroleum Science. Elsevier, pp. 109–118. https://doi.org/10.1016/B978-0-08-100404-3.00004-4

Sharma, P.V., 1997. Environmental and Engineering Geophysics. Cambridge University Press, Cambridge. https://doi.org/10.1017/CBO9781139171168

Singhal, B.B.S., 2008. Nature of hard rock aquifers: hydrogeological uncertainties and ambiguities, in: Ahmed, S., Jayakumar, R., Salih, A. (Eds.), Groundwater Dynamics in Hard Rock Aquifers: Sustainable Management and Optimal Monitoring Network Design. Springer, Dordrecht, The Netherlands, pp. 20–39. https://doi.org/10.1007/978-1-4020-6540-8_2

1149 Singhal, B.B.S., Gupta, R.P., 2010. Applied hydrogeology of fractured rocks, 2nd ed. Springer,
1150 Dordrecht, The Netherlands.

1151 Slater, L., 2007. Near surface electrical characterization of hydraulic conductivity: From
1152 Petrophysical Properties to Aquifer Geometries—A Review. Surv. Geophys. 28, 169–197.
1153 https://doi.org/10.1007/s10712-007-9022-y

1154 Tabibi, M., Emadi, M.A., 2013. Variable cementation factor determination (empirical methods).
1155 Presented at the SPE 13th Middle East Oil Show & Conference, Bahrain, p. 9.
1156 https://doi.org/10.1117/12.486983

1157 Taylor, R.G., Scanlon, B., Döll, P., Rodell, M., van Beek, R., Wada, Y., Longuevergne, L., Leblanc,
1158 M., Famiglietti, J.S., Edmunds, M., Konikow, L., Green, T.R., Chen, J., Taniguchi, M., Bierkens,
1159 M.F.P., MacDonald, A., Fan, Y., Maxwell, R.M., Yechieli, Y., Gurdak, J.J., Allen, D.M.,
1160 Shamsudduha, M., Hiscock, K., Yeh, P.J.-F., Holman, I., Treidel, H., 2013. Ground water and climate
1161 change. Nat. Clim. Change 3, 322–329. https://doi.org/10.1038/nclimate1744

1162 Tiab, D., Donaldson, E.C., 2016. Porosity and permeability, in: Petrophysics. Elsevier, pp. 67–186.
1163 https://doi.org/10.1016/B978-0-12-803188-9.00003-6

1164 Tiab, D., Restrepo, D.P., Igbokoyi, A.O., 2006. Fracture porosity of naturally fractured reservoirs, in:
1165 SPE-104056-MS. Presented at the International Oil Conference and Exhibition in Mexico, Society of
1166 Petroleum Engineers, Cancun, Mexico, p. 13. https://doi.org/10.2118/104056-MS

1167 Tokan-Lawal, A., Landry, C.J., Prodanovic, M., Eichhubl, P., 2014. Understanding tortuosity and
1168 permeability variations in naturally fractured reservoirs: Niobrara Formation, in: Proceedings of the
1169 2nd Unconventional Resources Technology Conference. Presented at the Unconventional Resources
1170 Technology Conference, American Association of Petroleum Geologists, Denver, Colorado, USA.
1171 https://doi.org/10.15530/urtec-2014-1922870

1172 Turesson, A., 2006. Water content and porosity estimated from ground-penetrating radar and
1173 resistivity. J. Appl. Geophys. 58, 99–111. https://doi.org/10.1016/j.jappgeo.2005.04.004

1174 Undul, O., Tugrul, A., Zarif, I., 2011. Identifying the weathering profiles of ultramafic rocks using
1175 electrical resistivity tomography (ERT), in: ARMA-11-172. Presented at the 45th U.S. Rock
1176 Mechanics / Geomechanics Symposium, American Rock Mechanics Association, ARMA, p. 10.

1177 Urish, D.W., 1981. Electrical resistivity-hydraulic conductivity relationships in glacial outwash
1178 aquifers. Water Resour. Res. 17, 1401–1408. https://doi.org/10.1029/WR017i005p01401

1179 Vereecken, H., 2006. Applied Hydrogeophysics, NATO science series. Springer, Dordrecht, The
1180 Netherlands.

1181 Vouillamoz, J.M., Sokheng, S., Bruyere, O., Caron, D., Arnout, L., 2012. Towards a better estimate of
1182 storage properties of aquifer with magnetic resonance sounding. J. Hydrol. 458–459, 51–58.
1183 https://doi.org/10.1016/j.jhydrol.2012.06.044

1184 Waxman, M.H., Smits, L.J.M., 1968. Electrical conductivities in oil-bearing shaly sands. Soc. Pet.
1185 Eng. J. 8, 107–122. https://doi.org/10.2118/1863-A

1186 Whitman, D., Yeboah-Forson, A., 2015. Electrical resistivity and porosity structure of the upper
1187 Biscayne Aquifer in Miami-Dade County, Florida. J. Hydrol. 531, 781–791.
1188 https://doi.org/10.1016/j.jhydrol.2015.10.049